Physical interactions reduce the power of natural selection in growing yeast colonies

Andrea Giometto[1,2,3], David R Nelson[1,2,3,4], Andrew W Murray[2,3]

1. Department of Physics, Harvard University, Cambridge, Massachusetts, United States of America
2. FAS Center for Systems Biology, Harvard University, Cambridge, Massachusetts, United States of America
3. Department of Molecular and Cellular Biology, Harvard University, Cambridge, Massachusetts, United States of America
4. School of Engineering and Applied Sciences, Harvard University, Cambridge, Massachusetts, United States of America

Abstract

Microbial populations often assemble in dense populations in which proliferating individuals exert mechanical forces on the nearby cells. Here, we use yeast strains whose doubling times depend differently on temperature to show that physical interactions among cells affect the competition between different genotypes in growing yeast colonies. Our experiments demonstrate that these physical interactions have two related effects: they cause the prolonged survival of slower-growing strains at the actively-growing frontier of the colony and cause faster-growing strains to increase their frequency more slowly than expected in the absence of physical interactions. These effects also promote the survival of slower-growing strains and the maintenance of genetic diversity in colonies grown in time-varying environments. A continuum model inspired by overdamped hydrodynamics reproduces the experiments and predicts that the strength of natural selection depends on the width of the actively-growing layer at the colony frontier. We verify these predictions experimentally.

Significance Statement

Microbes often live in dense populations such as colonies and biofilms. We show that the success and extinction of yeast strains within a growing colony are determined by a combination of their relative fitness and the forces exerted by proliferating cells on their neighbors. These physical interactions prolong the survival of less-fit strains at the growing frontier of the colony and slow down the colony's takeover by fitter strains. This reduction in the power of natural selection favors the maintenance of genetic diversity in environments in which the strains' relative growth rates vary with time. Growth-induced physical interactions may thus favor the maintenance of drug-resistant cells, which are typically less-fit than non-resistant cells, within dense microbial populations.

Keywords

spatial population genetics | selective sweeps | range expansion | evolution | extinction

Introduction

Life in the microbial world often occurs in crowded environments, such as colonies, biofilms, and tissues. Within such dense populations, cells compete for nutrients and space to survive, proliferate, and propagate their genotype to future generations. Classical results of population genetics theory on the competition between different genotypes in well-mixed populations (1) do not apply directly to these microbial aggregates, due to their growing size and spatial structure (2-9). Microbial range expansion experiments are a valuable tool for investigating ecological and evolutionary dynamics in spatial contexts (4, 5, 10-15) and extend our understanding of spatial population genetics (16). Early studies of microbial range expansions have shown that the growth of microbial colonies causes the spatial separation of genotypes (2), which makes theoretical models derived for well-mixed populations inapplicable. Biological interactions between genotypes can either reduce this segregation or increase it, depending on the nature of the interactions. For instance, Müller et al. (10) showed that mutualistic yeast strains cannot de-mix if they are obligate mutualists and thus depend on each other for growth. In contrast, McNally et al. (17) showed that antagonistic interactions among bacterial strains cause a phase separation that further increases the spatial separation of different strains. Although additional deviations from classical theory could be produced by the mechanical interaction between cells in dense populations, the effects of such interactions on microbial competition is still relatively unexplored. Among the few exceptions, Farrell et al. (18) showed that the physical properties of a cell can affect the dynamics of beneficial mutations in growing microbial colonies. They showed that the probability that a mutant spreads in the population can be related to summary statistics characterizing cell alignment and the roughness of the expanding front. In parallel to our investigation, Kayser et al. (19, 20) showed that the mechanical interaction between a faster-growing and a slower-growing strain can cause the prolonged survival of the slower-growing one, a process that we have investigated in a different geometry and from a different modeling perspective.

In this work, we study the effect of mechanical interactions among cells on the competition of strains in growing colonies of the budding yeast, *Saccharomyces cerevisiae*. We focus on the competition for space and for nutrients of two yeast strains with different fitnesses and study the dynamics of selective sweeps (the fitter strain's increase in relative frequency at the frontier of the expanding colony) and the local extinction dynamics of the less-fit strain. We find that mechanical interactions reduce the strength of natural selection by slowing down the extinction of slower-growing strains and by reducing the rate at which faster-growing ones increase their frequency within a population. We show that a continuum model inspired by overdamped hydrodynamics can reproduce the experimental data and make new predictions that we verify experimentally. Specifically, the model predicts that the speed at which selective sweeps spread in a growing colony is inversely related to the width of the actively growing layer at the colony frontier. We tested the model by co-culturing two yeast strains with different temperature-dependent growth profiles. We show that the prolonged survival of the less-fit strain, which occurs via the formation of thin, persistent filaments (Fig. 1A-A2), promotes the maintenance of genetic diversity in the population when two strains compete in an environment in which their relative growth rates vary with time. This reduction in the efficiency of natural selection may be beneficial for microbial populations by delaying the extinction of slower-growing genotypes which carry traits that can later be beneficial for the population, such as resistance to antimicrobial drugs.

Results

When two yeast strains are mixed and inoculated as a drop on a solid nutrient medium, they form a mixed-strain colony that expands radially with time. A well-known feature of such colony expansion is the spatial de-mixing of strains due to genetic drift (2), which forms single-strain sectors. When one strain expands faster than the other, the size of its sectors increases with time (5) (Fig. 1A). We performed colony-growth experiments using two *S. cerevisiae* strains with different doubling times. As expected, single-strain colonies of the strain (yAG2) with the shorter doubling time expanded faster than single-strain colonies of the strain (yAG1) with the longer doubling time. We found that single-strain sectors within mixed colonies interact mechanically in ways that affect the competition between the two strains. These mechanical interactions are visible in Fig. 1A. At each side of sweeping sectors of the faster-growing (yellow) strain, the slower-growing (blue) strain was displaced and pulled towards the exterior of the colony (Fig. 1A-A1). Occasionally, the slower-growing strain was trapped between two sectors of the faster-growing one in the early phases of the expansion and traveled longer distances (blue filaments in Fig. 1A-A2) than in other regions of the colony, where the slower-growing strain was farther from the faster-growing strain. The enhanced expansion of the slower-growing strain occurs as a thin, persistent filament that originates via a combination of cell division and the physical interactions with the faster-growing strain, the most prominent of which is the pressure exerted by proliferating cells on their neighbors. The prolonged survival of these filaments is favored by the small fluctuations of the filament boundaries relative to the filament thickness (SI section 3 and Fig. S3). The formation of a thin, persistent filament depends on the spatial distribution of the two strains after de-mixing. If a thin, slower-growing sector is trapped between two faster-growing sectors, whose boundaries are nearly perpendicular to the frontier of the colony, the slower-growing sector is maintained as a thin filament. In contrast, if the two faster-growing sectors are initially far apart, their edges meet subtending a substantial angle (>20°) and pinch off the slower-growing sector (Fig. 4B and Fig. S1). This phenomenon leads to the counterintuitive result that a small sector of the slower-growing strain that is initially bounded on both sides by the faster-growing strain can survive for longer times, as a thin, persistent filament, than a larger sector of the slower-growing strain.

We wanted to rule out the possibility that persistent filaments were due to the ability of the faster-growing strain to speed up (for example, via chemical secretions) the proliferation of cells of the slower-growing strain that were nearby. We therefore produced mixed colonies from two strains: a wild-type strain that proliferated at temperatures from 20 to 37°C (yAG19, cyan in Fig. 1B-C) and a strain carrying a temperature-sensitive mutation that could only proliferate at temperatures below 30°C (yAG20, magenta in Fig. 1B-C). To ask if the formation of persistent filaments required the proliferation of the less-fit strain, we imposed the extreme condition of preventing the proliferation of the less fit strain. The heat-sensitive strain used here is a *cdc26Δ* mutant that arrests in mitosis and therefore cannot complete the cell division cycle at temperatures above 30°C (21). We grew single-strain and mixed-strain colonies of these two strains at 28°C for two days and subsequently imaged them with a stereoscope incubated at 37°C for 23 h. We observed that single-strain, heat-sensitive colonies stopped expanding after 9 h from the start of the measurement (Fig. 1B and Fig. S2). In the following hours, single-strain sectors of the non-heat-sensitive strain emerged from the mixed colony, displacing the heat-sensitive strain and producing patterns (Fig. 1C-C1) that are visually similar to those shown in Fig. 1A. Specifically, the non-dividing heat-sensitive strain was nevertheless displaced on each side of sweeping sectors of the non-heat-

sensitive one and sectors of the heat-sensitive strain trapped between two sectors of the other strain (Fig. 1C1) were squeezed and formed filaments that resemble those shown in Fig. 1A-A2. Because the heat-sensitive single-strain colonies were not expanding when non-heat-sensitive sectors emerged from the mixed-strain colony (Fig. S2D), the displacement of the heat-sensitive strain was caused by the physical interaction between the two strains.

The experiments described above show that mechanical interactions cause the prolonged survival of the slower-growing strain in mixed-strain colonies, via thin, persistent filaments trapped between sweeping sectors of the faster-growing strain. To highlight the effect of this persistence on the competitive dynamics of strains in growing colonies, we designed a colony-growth experiment in which we could use environmental switches to alternate which strains grew faster and slower. The strain yAG2 is cold-sensitive due to the *trp1-1* mutation, which requires it to import tryptophan from the medium, a process whose efficiency is reduced at lower temperatures (22), so that yAG1 grows faster than yAG2 at low temperatures and more slowly at high temperatures. At 12˚C, single-strain colonies of yAG1 expanded faster (0.288$\pm$0.004 mm/d) than those of yAG2 (0.226$\pm$0.010 mm/d), whereas at 30˚C single-strain colonies of yAG2 expanded faster (1.15$\pm$0.02 mm/d) than those of yAG1 (0.96$\pm$0.03 mm/d). Thus, by changing the temperature during a mixed-strain colony growth experiment, we could control which strain was proliferating faster. We performed mixed-strain colony growth experiments starting from a 50%-50% mixture of yAG1 and yAG2 and incubated these colonies at 30˚C at the start of the experiment, then moved the colonies to 12˚C after a few days, and moved them again to 30˚C towards the end of the experiment (Methods). The duration of each temperature phase varied between different replicates. Fig. 2 and Figs. S4-S6 show that strains can survive as persistent, thin filaments at the temperature where they grow slower and then expand in the next phase, at a temperature where they grow faster than their competitor.

We made a hydrodynamic model to describe the observed interactions between strains at the macroscopic scale (i.e., at scales much larger than the typical cell diameter). Our model for the dynamics of the competition between two strains in growing colonies used a two-dimensional continuum description based on overdamped hydrodynamics. This approach is valid on time scales that are long compared to a cell division time and length scales that are large compared to a cell diameter and to the colony height near the frontier. We first describe the model for a single-strain colony and then generalize it to the case of multiple strains. Let $\rho(x, y, t)$ be the two-dimensional density (with dimensions of cells/length^2) of a single-strain colony at time t, where x and y are cartesian coordinates on the agar plane. If h is the height of the colony, we have $\rho = h\rho_{3d}$, where we assume that the three-dimensional density ρ_{3d} (with dimensions of cells/length^3) is constant within the colony. Because experimental colonies are approximately flat in the direction parallel to the agar surface close to the frontier, we will assume that h (and thus ρ) is also constant within the colony, and equal to zero outside. Let $g(x, y, t)$ be the local growth rate (with dimensions of 1/time) of yeast cells at time t. Experimental observations reveal that the spatial distribution of strains in mixed-strain colonies is time-invariant at distances larger than 500 μm (about 100 cell diameters) behind the colony frontier (Fig. S7), indicating that cell divisions that affect the visible surface of the colony take place mostly within this distance from the frontier. This observation led us to define a distance δ from the frontier of the colony such that $g(x, y, t) = \bar{g}$, with constant $\bar{g} > 0$, for every point (x, y) inside the colony within a distance δ from the frontier at time t, and $g(x, y, t) = 0$ for every other point. With these assumptions, the radial expansion speed of a circular single-strain colony is equal to $\bar{v} = dr/dt = \bar{g}\delta[1 - \delta/(2r)] \cong \bar{g}\delta$ (SI Methods), where

the last approximation is justified because typically $\delta \ll r$ in colony-growth experiments. The considerations made above translate into the following hydrodynamic partial differential equations for the two-dimensional colony density ρ:

$$\frac{\partial \rho}{\partial t} + \vec{\nabla} \cdot (\rho \vec{v}) = \rho g, \tag{1}$$

and

$$\vec{\nabla} \cdot \vec{v} = g, \tag{2}$$

where Eq. 1 generalizes the usual continuity equation (the position-dependent growth rate g appears as a source term), $\vec{v}$ is the two-dimensional velocity field within the colony, $\vec{\nabla}$ is the gradient operator and $\vec{\nabla} \cdot \vec{v}$ is the divergence of $\vec{v}$. Eq. 2 enforces mass conservation within the colony along a streamline, ensuring that the two-dimensional density ρ is constant within the colony. Upon neglecting inertial terms because the dynamics is overdamped, the momentum equation reads:

$$\vec{\nabla} p = \mu \nabla^2 \vec{v} - \gamma \vec{v}, \tag{3}$$

where ∇^2 is the two-dimensional Laplacian operator, μ is the dynamic viscosity of the colony, γ is the frictional drag supplied to the colony by the substrate and $p(x, y, t)$ is the two-dimensional pressure field within the colony at time t. Under our experimental conditions, the term $\mu \nabla^2 \vec{v}$ can be neglected relative to $\gamma \vec{v}$, so that Eq. 3 becomes:

$$\vec{\nabla} p = -\gamma \vec{v}, \tag{4}$$

which says that the velocity $\vec{v}$ with which strains are displaced within the colony is proportional to the pressure gradient $\vec{\nabla} p$. Eqs. 1, 2 and 4 have been used previously to model biofilm growth (23). We show in the SI section 8 that they can be derived from the three-dimensional continuity and Navier-Stokes equations by adopting the lubrication approximation (24), which gives the value of the friction-like coefficient $\gamma = 2\mu/h^2$ in terms of the colony dynamic viscosity μ and the colony height h. The approximation is appropriate when $\delta \gg h/\sqrt{2}$, that is, when the height of the colony is small compared with the growth layer width, as found experimentally ($\sqrt{2}\delta/h \cong 20$). We are also justified in neglecting the viscosity term in Eq. 3 in this limit. Upon taking the divergence of Eq. 4 and using Eq. 2, one finds:

$$\nabla^2 p = -\gamma \vec{\nabla} \cdot \vec{v} = -\gamma g, \tag{5}$$

that is, the pressure field within the colony satisfies a Poisson equation. Yeast cells attract each other mildly (25), and these attractive forces could give rise to line tension terms causing a pressure discontinuity at the colony frontier, with the magnitude of the discontinuity proportional to the local curvature of the frontier. In our experimental settings, however, line tension terms are negligible (see SI section 10 and Fig. S11), and thus we can set the boundary condition $p = p_0$ at the outer edge of the colony, where p_0 is a constant reference pressure (because the value of p_0 does not affect the dynamics, we set $p_0 = 0$). This simple model can be generalized to mixed-strain colonies by considering two different two-dimensional densities $\rho_1(x, y, t)$ and $\rho_2(x, y, t)$, giving the density of each strain. Given the sharp boundaries between the two strains observed in colony growth experiments (see, e.g., Fig. 1A), we assume that the two strains cannot simultaneously occupy the same position in space at the same time t, so that for each point (x, y)

within the colony either ρ_1 or ρ_2 must be equal to zero, and the colony density is equal to $\rho = \rho_1 + \rho_2$. In the same way, the local growth rate is equal to $g = g_1 + g_2$ within the colony, where either g_1 or g_2 must be equal to zero, according to which strain occupies the position (x, y) at time t. With this definition of g, the overall pressure and velocity fields within the mixed-strain model are still given by Eqs. 4 and 5. Note that, because pressure is proportional to γ (Eq. 5) and the velocity field is given by $\vec{v} = -\vec{\nabla}p/\gamma$ (Eq. 4), the frictional coefficient γ drops out and does not affect the displacement of strains within the colony and thus its spatio-temporal dynamics.

We find that simulations based on this continuum model can reproduce the experimental observation of the mechanical interaction of single-strain sectors within growing colonies (Fig. 4B), namely the displacement of the slower-growing strain in the proximity of a faster-growing sector and the prolonged survival and enhanced expansion speed of thin filaments of the slower-growing strain trapped between two sectors of the faster-growing one (Fig. 4B). Both these effects become more pronounced as the width, δ, of the growth layer increases. Note that the same observations are not predicted by a constant-speed model (5) inspired by geometrical optics in which each strain advances at a constant speed, perpendicular to the frontier of the colony (Fig. 4A). The constant-speed model is known to fail for the early dynamics of sweeping sectors (e.g., for sectors composed of individuals with beneficial mutations), for example when the two walls bounding such sectors are close to each other (5). The temporal dynamics of a sweeping sector can be quantified by its opening angle, which is defined as the angle formed by the two lines connecting the center of the inoculum to the boundary between the two strains at the frontier of the colony (e.g., the angle ϕ in Fig. 1A and inset of Fig. 3A). In the constant-speed model, the sector boundaries form logarithmic spirals, with their opening angle increasing logarithmically with the radius of the colony (5). In simulations of the continuum model, however, the dynamics of opening angles can be separated into two stages, which are best seen on a log-linear scale (continuous lines in Fig. 3D). Initially, opening angles increase exponentially with the radius r, defined at the point in which the two strains meet at the frontier of the colony (Fig. 3A, inset). At later times (or, equivalently, larger radii r), the rate of increase of sweeping sector opening angles versus r eventually tends to the constant-speed model prediction (Fig. 3D and Fig. S13), that is, opening angles increase logarithmically with r. We find that the continuum model results tend to the constant-speed model ones as the width of the growth layer δ tends to zero, while keeping the constant asymptotic expansion speed $\bar{v}_i = \bar{g}_i\delta$ of each strain i constant by varying $\bar{g}_i$ (Fig. S13). This observation makes sense because the constant-speed model, which is inspired by geometrical optics, assumes that each point at the colony frontier (corresponding to an extremely narrow growth layer) is the source of a circular growth wave in the infinitesimal time interval dt, and that the outline of the colony at time $t + dt$ is given by the envelope of such waves (5).

We tested whether our continuum model could reproduce the observed temporal evolution of the opening angles of sweeping sectors. We performed colony growth experiments at 30˚C with the slower-growing strain yAG1 and the faster-growing strain yAG2 and measured the opening angles of sweeping yAG2 sectors that remained far from each other throughout the entire experiment (e.g., the four isolated yellow sectors at 2, 8, 9 and 11 o' clock in Fig. 1A). Opening angles measured at different times and colony radii are shown in Fig. 3A-B and Fig. S8. We grouped the experimentally-measured opening angle trajectories of sweeping yAG2 sectors into two classes (small and large angles), based on the opening angle of each sector at the second measurement point, which was taken as the initial condition for the comparison with the models (see SI section 6 for an explanation). A log-linear plot highlights the initial exponential dependence of opening

angles on the distance from the center of the colony to the points at which yAG1 and yAG2 sectors meet at the frontier of the colony (Fig. 3B). The constant-speed model (dashed lines in Fig. 3A-B, based on each strain's expansion velocity measured in single-strain colony growth experiment), strongly overestimates the initial increase in the opening angles of sweeping yAG2 sectors. We tested if our continuum model could reproduce the experiments by fitting the continuum model to the experimental opening angles of sweeping sectors. The expansion velocities $\bar{v}_1$ and $\bar{v}_2$ measured in single-strain colony growth experiments constrained the products $\bar{g}_1\delta = \bar{v}_1$ and $\bar{g}_2\delta = \bar{v}_2$ in the continuum model, assuming an identical growth layer width δ for the two strains. Thus, we could vary the width δ of the growth layer in the model ($\bar{g}_1$ and $\bar{g}_2$ were then uniquely determined) and use it as a parameter to fit the sector opening angles. The resulting model fit is shown in Fig. 3A-B (continuous lines). The best-fit estimate is δ=320$\pm$40 μm. We experimentally measured the characteristic length-scale over which growth affects the visible surface of yeast colonies and found it to be equal to δ_{exp}=530±120 μm (mean±SD, see SI section 5 and Fig. S7). The best-fit estimate of δ is smaller than δ_{exp}, but this is not surprising (see SI section 5) given that the colony height goes to zero at the colony frontier, whereas the model assumes constant height everywhere.

The continuum model predicts that the opening angles of sweeping sectors increase faster for smaller values of δ. To test this prediction, we reduced the value of the growth layer width δ by reducing the wetness of the agar plates and measured the dynamics of the opening angles of sweeping sectors in this condition (Fig. 3C-D). We experimentally verified that the growth layer width was reduced, compared to wetter plates (SI section 5 and Fig. S7). In the experiment with a narrower growth layer width, even though the ratio of the expansion velocities (Fig. S9) of the two single strains ($\bar{v}_2/\bar{v}_1$=1.17$\pm$0.06) was slightly smaller than in the experiment with wider growth layer width ($\bar{v}_2/\bar{v}_1$=1.23$\pm$0.05), the opening angles increased more rapidly, consistent with the smaller growth layer width δ, thus verifying the continuum model's prediction. Although the constant-speed model fails to predict correctly the early time dynamics of opening angles, it does a better job than for the previous experiment, as expected given the smaller value of δ and our observation that the continuum model tends to the constant-speed model in the limit $\delta \to 0$. As in the previous experiment, our continuum model can reproduce the experimental dynamics of sweeping sector opening angles by fitting the growth layer width to the data (Fig. 3C-D, continuous lines). The best-fit parameter for this experiment is δ=95$\pm$10 μm. In this case, one can observe the transition from the exponential (for small ϕ and small r) to logarithmic dependence of ϕ on r predicted by our continuum model (Fig. 3C-D). Such a transition is not discernible (or barely so) in the experiment described in the previous paragraph (Fig. 3A-B), due to the larger value of the growth layer width δ for wetter plates.

Discussion

Our experiments show that physical (pressure-induced) interactions between yeast strains within growing colonies reduce the efficiency of natural selection both by allowing less fit strains to persist and by slowing down the expansion of fitter strains. Slower-growing strains expand faster in parts of the colony that are close to faster-growing strains. When a slower-growing strain is trapped in a thin gap between two sectors of the faster-growing one, it expands at almost the same speed as the latter and forms a persistent thin filament that can survive for very long times. In addition, physical interactions slow the initial dynamics of selective sweeps compared to the expectation of the constant-speed model, which assumes that the strains expand independently of each other except that two strains cannot occupy the same position. The magnitude of these effects

increases with the width δ of the actively-growing layer at the frontier of the expanding colony. Our continuum model gives us an intuition for the physical origin of the experimental observations. Thin, persistent filaments are pushed towards the exterior of the colony by the surrounding faster-growing strain and benefit from the pressure field generated by the latter. Conversely, sweeping sectors of the faster-growing strain that have small initial opening angles are too small to generate enough pressure and thus initially expand more slowly than the predictions of the constant-speed model. Even though our continuum model is deterministic and thus cannot reproduce the stochastic extinction of small sectors of the faster-growing strain, which are sometimes observed in the experiments (see, e.g., Fig. 1A), it helps us to understand why such extinctions can occur. Sectors of the faster-growing strain initially expand at approximately the same speed as the surrounding slower-growing strain, making the competition between the two strains almost neutral, somewhat enhancing the importance of stochastic effects. Our experiments in time-varying environments show that the existence of thin, persistent filaments can play an important role in determining the outcome of competition between strains. In environments that fluctuate between two environmental states in which each strain has a selective advantage over the other one, the persistent filaments facilitate survival during detrimental environmental states and allow immediate recovery once the relative advantage of the two strains is reversed.

Because the reduced efficiency of natural selection described here is due to physical forces acting within dense cell populations, we believe such effects are relevant for a broad range of biological systems. We expect that the observed reduction in the effective selective advantage of a fitter strain (when sector widths are small) should be relevant for beneficial mutations that arise in a colony and manage to establish a clonal sector. In the initial phase of their dynamics, such sectors will expand at approximately the same rate as the surrounding wild type cells, and the expansion speed of the beneficial mutation will increase as its sector grows wider. This size-dependent selective advantage of a fitter strain or beneficial mutation is reminiscent of positive frequency-dependent selection (26), in which the fitness of a genotype increases with its frequency in the population. In the context of our work, the frequency dependence is caused by the pressure field induced by cell division. Experimental (27) and theoretical (28) studies have shown that populations undergoing range expansion accumulate deleterious mutations as a result of consecutive founder events and genetic drift being stronger at the frontier in spatial (compared to well-mixed) populations, due to their reduced effective population sizes. Our work suggests that deleterious mutations have higher chances of being maintained in dense, expanding microbial populations than expected based on genetic drift alone, because the effects of differences in fitness are reduced by physical interactions. Our findings are relevant for the fate of drug-resistant mutations that arise in microbial colonies or biofilms. Such mutations are typically associated with fitness deficits. Our work suggests that drug-resistant mutants (e.g., antibiotic-resistant bacteria) emerging in the outer layer of an expanding colony may benefit from the physical interaction with the surrounding wild-type cells and survive for long times in the actively-dividing frontier of the colony in the absence of the drugs that they confer resistance to. The application of a drug would reverse the relative fitness of drug-resistant mutants and wild-type cells and allow the drug-resistant mutant to take over the population, similar to our experiments where temperature varies in time for temperature-sensitive strains. We thus expect that the physical interactions between different genotypes investigated here would favor the maintenance of genetic diversity within dense microbial populations and allow such populations to withstand time-dependent fluctuations of the environment or the application of antimicrobial drugs. Finally, our findings may extend beyond microbial populations and inform us about the dynamics of pre-vascular tumor growth (7, 29). Within tumors, various cell lineages

compete for space and form spatially-coherent clusters that are reminiscent of the genetic de-mixing found in colony-growth experiments (30). A recent study (30) has shown that individual tumors can have high levels of genetic diversity and argued that such high-diversity levels can only be explained by non-Darwinian selection, i.e., neutral competition between different clones. The reduced efficiency of natural selection highlighted here, transposed to the three dimensional environment at the frontier of a spherical cell cluster, is one possible mechanism to explain the apparent neutrality of inter-clone competition within such tumors.

Methods

Strains. The genotypes of all strains used in this study are reported in Table S1. In the fluorescent images throughout this paper, yAG1 is portrayed in blue, yAG2 in yellow, yAG19 in cyan and yAG20 in magenta.

Colony-growth experiments. Colony-growth experiments were conducted on 1% agarose plates with YPD (Yeast extract-Peptone-Dextrose) medium at 30˚C, unless otherwise stated. Plates were poured two days before inoculation and stored at room temperature. Strains were pre-grown at 30˚C overnight in liquid YPD. Before inoculation on agarose plates, 200 μL of each overnight culture were spun down for 1 min at 9400 g and re-suspended in 1 mL of 1% PBS (Phosphate-Buffered saline). The densities of such suspensions were measured with a Coulter Counter and brought to a density of $3{\cdot}10^7$ cells/mL by adding 1% PBS or removing the supernatant in appropriate amounts. If required, suspensions were mixed in the desired ratios. A 0.6 μL droplet was pipetted on each agarose plate. Further details that varied between experiments are discussed below.

Sweeping sectors dynamics experiment. We performed two sets of experiments to measure the dynamics of sweeping yAG2 sectors at different growth layer widths. For the first set of experiments (wide growth layer), we poured 7 mL YPD 1% agarose medium into Petri dishes with a diameter of 35 mm. After one day from pouring, solidified YPD agarose discs were transferred to larger Petri dishes with diameters of 100 mm, three discs for each larger dish. One droplet of either a single-strain or a mixed-strain suspension (relative frequencies of yAG1 and yAG2 were 99% and 1%, respectively) was inoculated on the surface of each disc. After inoculation, 7 mL of liquid YPD medium were added to the Petri dish, and spread over the empty space between the discs. The liquid medium was substituted daily to ensure that the nutrients available to each colony did not become depleted. Colonies were imaged twice per day with a Zeiss Lumar stereoscope. For the second set of experiments (narrow growth layer), we poured 33 mL YPD 1% agarose medium into Petri dishes with a diameter of 100 mm. One droplet of either a single-strain or a mixed-strain suspension (relative frequencies of yAG1 and yAG2 were 99% and 1%, respectively) was inoculated on the surface of each plate. Plates were incubated at 30˚C for the whole duration of the experiments. Colonies were imaged once per day with a Zeiss Lumar stereoscope.

Radial expansion velocities. Single-strain colony radii were measured by fitting circles to each single-strain colony bright-field image using the software ImageJ. Radial expansion velocities were computed by fitting the radius-vs-time data to straight lines, separately for each colony. The mean radial expansion velocity of each strain was computed as the mean slope of the radius-vs-time fits. For the wide growth layer experiment, yAG1 and yAG2 expansion velocities were measured across 10 and 9 single-strain colonies, respectively. The mean radii at different times are shown in Fig. S9A. The measured velocities were $\bar{v}_1$=1.89±0.04 mm/d (mean±SD) and $\bar{v}_2$=2.33±0.09 mm/d (mean±SD). For the narrow growth layer experiment, yAG1 and yAG2

expansion velocities were measured across 11 single-strain colonies for each strain. The mean radii at different times are shown in Fig. S9C. The measured velocities were $\bar{v}_1$=1.08±0.04 mm/d (mean±SD) and $\bar{v}_2$=1.26±0.04 mm/d (mean±SD).

cdc26Δ mutant experiments. We performed colony-growth experiments with the strains yAG19 and yAG20 to show that the interactions between single-strain sectors are due to the mechanical interaction of strains within growing colonies. These experiments were done with 100 mm Petri dishes filled with 33 ml of 1% agarose YPD medium. We grew single-strain and mixed-strain colonies of yAG19 and yAG20 for two days at 28˚C and subsequently moved them to the stage of a stereoscope incubated at 37˚C. Colonies were imaged every 10 min for 23 h. The same experiment was performed with yAG2 and yAG20 single-strain and mixed-strain colonies and the results do not differ qualitatively. We verified that yAG20 cells recovered from single-strain colonies grown at 37˚C do not complete the cell cycle and form buds that grow to be as large as the mother cells (21).

Time-varying temperature experiments. We performed time-varying temperature experiments with 100 mm Petri dishes filled with 33 mL of 1% agarose YPD medium. We inoculated 11 plates with a mixed-strain 0.6 μL droplet (the relative frequencies of yAG1 and yAG2 were 50% and 50%). Among these plates, three were incubated at 30˚C for 2 days, then at 12˚C for 9 days and then at 30˚C for 14 days (Fig. S4). Three plates were incubated at 30˚C for 3 days, then at 12˚C for 16 days and then at 30˚C for 10 days (a colony grown on one of these plates is shown in Fig. 2A-C, all three are shown in Fig. S5). Three plates were incubated at 30˚C for 3 days, then at 12˚C for 20 days and then at 30˚C for 9 days (Fig. S6). One plate was incubated at 30˚C for 13 days and then at 12˚C for 18 days (Fig. 2D-L). We inoculated 6 plates with a 0.6 μL droplet of yAG1. Three of these plates were stored at room temperature overnight and then moved to a 12˚C incubator for the whole duration of the experiment. The remaining three plates were placed in a 30˚C incubator for the whole duration of the experiment. We inoculated 6 plates with a single-strain yAG2 0.6 μL droplet and divided them in two triplets as described for the yAG1 plates. We took fluorescent and bright-field images of these plates after one day from inoculation, on each day in which we moved the mixed-strain plates between incubators with different temperatures, and a few other times between temperature changes. The single-strain colonies were used to measure single-strain radial expansion velocities at the two temperatures.

Continuum and constant-speed models. The overdamped fluid-dynamics (continuum) and the constant-speed models were solved numerically using level-set methods (31) and isotropic discrete operators from lattice hydrodynamics (32). Details on the numerical implementation of the models are in the SI Methods.

Acknowledgements

AG thanks Sauro Succi for helpful discussions on the numerical integration of the continuum model. We thank the members of the AWM and DRN groups for valuable suggestions. AG was supported by a research fellowship from the Swiss National Science Foundation, project P2ELP2_168498 and work on this project was supported by the Human Frontiers Science Program Grant RGP0041/2014 to AWM and DRN. Work by AG and DRN was supported by the National Science Foundation, through grants DMR1608501 and via the Harvard Materials Science Research and Engineering Center via grant DMR1435999.

References

1. Crow JF, Kimura M (2009) *An Introduction to Population Genetics Theory* (Blackburn Press, Caldwell, NJ).
2. Hallatschek O, Hersen P, Ramanathan S, Nelson DR (2007) Genetic drift at expanding frontiers promotes gene segregation. *Proc Natl Acad Sci U S A* 104:19926-19930.
3. Hallatschek O, Nelson DR (2009) Population genetics and range expansions. *Phys Today* 62:42-47.
4. Hallatschek O, Nelson DR (2010) Life at the front of an expanding population. *Evolution* 64:193-206.
5. Korolev KS, *et al*. (2012) Selective sweeps in growing microbial colonies. *Phys Biol* 9:026008.
6. Weinstein BT, Lavrentovich MO, Moebius W, Murray AW, Nelson DR (2017) Genetic drift and selection in many-allele range expansions. *PLoS Comput Biol* 13:e1005866.
7. Lavrentovich MO, Nelson DR (2015) Survival probabilities at spherical frontiers. *Theor Popul Biol* 102:26-39.
8. Kimura M, Weiss GH (1964) The stepping stone model of population structure and the decrease of genetic correlation with distance. *Genetics* 49:561-576.
9. Excoffier L, Foll M, Petit RJ (2009) Genetic consequences of range expansions. *Annu Rev Ecol Evol Syst* 40:481-501.
10. Muller MJI, Neugeboren BI, Nelson DR, Murray AW (2014) Genetic drift opposes mutualism during spatial population expansion. *Proc Natl Acad Sci U S A* 111:1037-1042.
11. Van Dyken JD, Muller MJI, Mack KML, Desai MM (2013) Spatial population expansion promotes the evolution of cooperation in an experimental prisoner's dilemma. *Curr Biol* 23:919-923.
12. Weber MF, Poxleitner G, Hebisch E, Frey E, Opitz M (2014) Chemical warfare and survival strategies in bacterial range expansions. *J R Soc Interface* 11:20140172.
13. Nadell CD, Drescher K, Foster KR (2016) Spatial structure, cooperation and competition in biofilms. *Nat Rev Microbiol* 14:589-600.
14. Giometto A, Rinaldo A, Carrara F, Altermatt F (2014) Emerging predictable features of replicated biological invasion fronts. *Proc Natl Acad Sci U S A* 111:297-301.
15. Giometto A, Altermatt F, Rinaldo A (2017) Demographic stochasticity and resource autocorrelation control biological invasions in heterogeneous landscapes. *Oikos* 125(11):1554-1563.
16. Korolev KS, Avlund M, Hallatschek O, Nelson DR (2010) Genetic demixing and evolution in linear stepping stone models. *Rev Mod Phys* 82:1691-1718.
17. McNally L, *et al*. (2017) Killing by Type VI secretion drives genetic phase separation and correlates with increased cooperation. *Nat Commun* 8:14371.
18. Farrell FF, Gralka M, Hallatschek O, Waclaw B (2017) Mechanical interactions in bacterial colonies and the surfing probability of beneficial mutations. *J R Soc Interface* 14:20170073.
19. Kayser J, Schreck C, Gralka M, Fusco D, Hallatschek O (2018) Collective motion conceals fitness differences in crowded cellular populations. *bioRxiv* 267286.
20. Hallatschek O (2018) H49.00006. Emergent evolutionary dynamics in dense cellular populations. *APS March Meeting 2018*.
21. Hwang LH, Murray AW (1997) A novel yeast screen for mitotic arrest mutants identifies DOC1, a new gene involved in cyclin proteolysis. *Mol Biol Cell* 8(10):1877-1887.

22. Singh A, Manney TR (1974) Genetic-analysis of mutations affecting growth of Saccharomyces-cerevisiae at low-temperature. *Genetics* 77(4):651-659.
23. Klapper I, Dockery J (2002) Finger Formation in Biofilm Layers. *SIAM Journal on Applied Mathematics* 62:853-869.
24. Batchelor GK (2000) *An Introduction to Fluid Dynamics* (Cambridge University Press, Cambridge).
25. Nguyen B, Upadhyaya A, Van Oudenaarden A, Brenner MP (2004) Elastic instability in growing yeast colonies. *Biophys J* 86:2740-2747.
26. Prout T (2001) Frequency-Dependent Selection. *Encyclopedia of Genetics*, eds Brenner S, Miller JH (Academic Press), Vol 1, pp 730-731.
27. Bosshard L, *et al*. (2017) Accumulation of deleterious mutations during range expansions. *Genetics* 207:669-684.
28. Peischl S, Dupanloup I, Kirkpatrick M, Excoffier L (2013) On the accumulation of deleterious mutations during range expansions. *Mol Ecol* 22:5972-5982.
29. Korolev KS, Xavier JB, Gore J (2014) Turning ecology and evolution against cancer. *Nat Rev Cancer* 14:371-380.
30. Ling SP, *et al*. (2016) Extremely high genetic diversity in a single tumor points to prevalence of non-Darwinian cell evolution. *Proc Natl Acad Sci U S A* 112(47):E6496-E6505.
31. Osher S, Fedkiw RP (2003) *Level set methods and dynamic implicit surfaces* (Springer, New York).
32. Thampi SP, Ansumali S, Adhikari R, Succi S (2013) Isotropic discrete laplacian operators from lattice hydrodynamics. *J Comput Phys* 234:1-7.

Figures

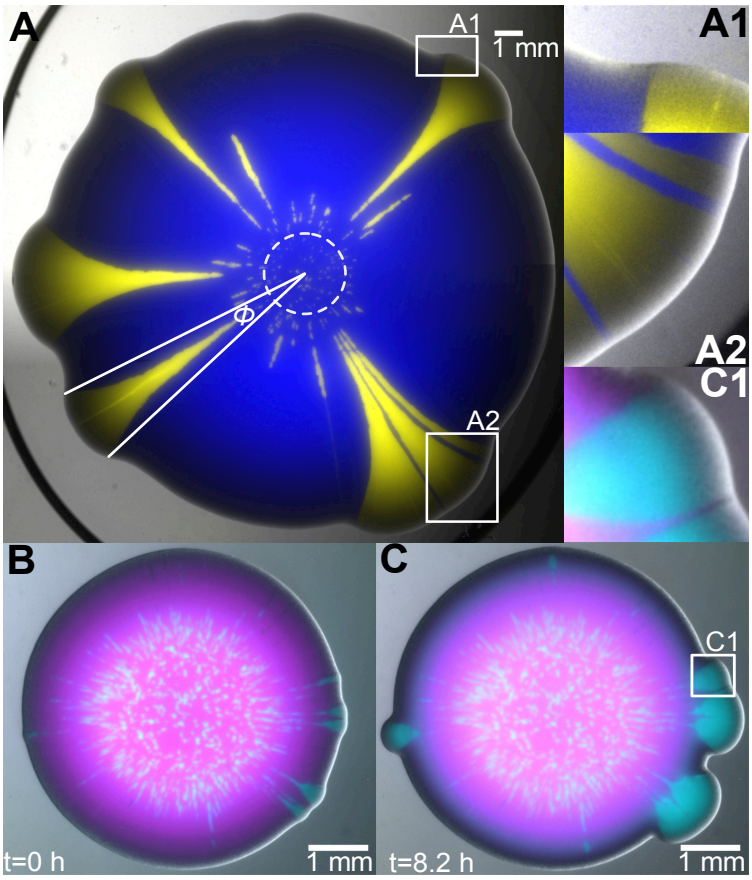

Fig. 1. *S. cerevisiae* colony-growth experiments hint at physical interactions between strains. (A) Combined fluorescent and bright-field image of a colony, four days after the inoculation of a mixed droplet of strains yAG1 (blue) and yAG2 (yellow) at relative frequencies of 99% and 1%, respectively, grown at 30˚C. The white dashed circle marks the spatial extent of the inoculum. Because yAG2 divides faster at 30˚C, some single-strain yellow sectors expand their opening angle ϕ as the colony grows radially, while others go extinct due to stochastic effects in the early stages of colony growth. By expanding faster, the faster-growing strain displaces the other strain at both sides of yellow sectors (A1) and can enhance the expansion speed of the slower-growing strain when it is trapped between two yellow sectors (blue filaments in A2) and is carried along. (B-C) Even non-proliferating cells (magenta) can be pulled outwards by a proliferating (cyan) strain. The images show combined fluorescent and bright-field images of the same colony at early and later times. In this experiment, the non-heat-sensitive strain yAG19 (cyan, initial frequency 10%) and the heat-sensitive strain yAG20 (magenta, initial frequency 90%) were grown at 28˚C for two days and subsequently imaged with a stereoscope incubated at 37˚C, a temperature at which yAG20 cells cannot divide. Panel B shows the first snapshot (determined experimentally, see Fig. S2D) at which the heat-sensitive strain stopped expanding. Panel C shows the colony after a further 8.2 h. (C1) Close-up of the region marked with a white square in C, highlighting the displacement of the non-growing, heat-sensitive strain next to expanding sectors of the growing strain and an expanding magenta filament trapped between two cyan sectors. Because the heat-sensitive strain did not divide between B and C, its displacement can only be due to the physical interaction between the two strains.

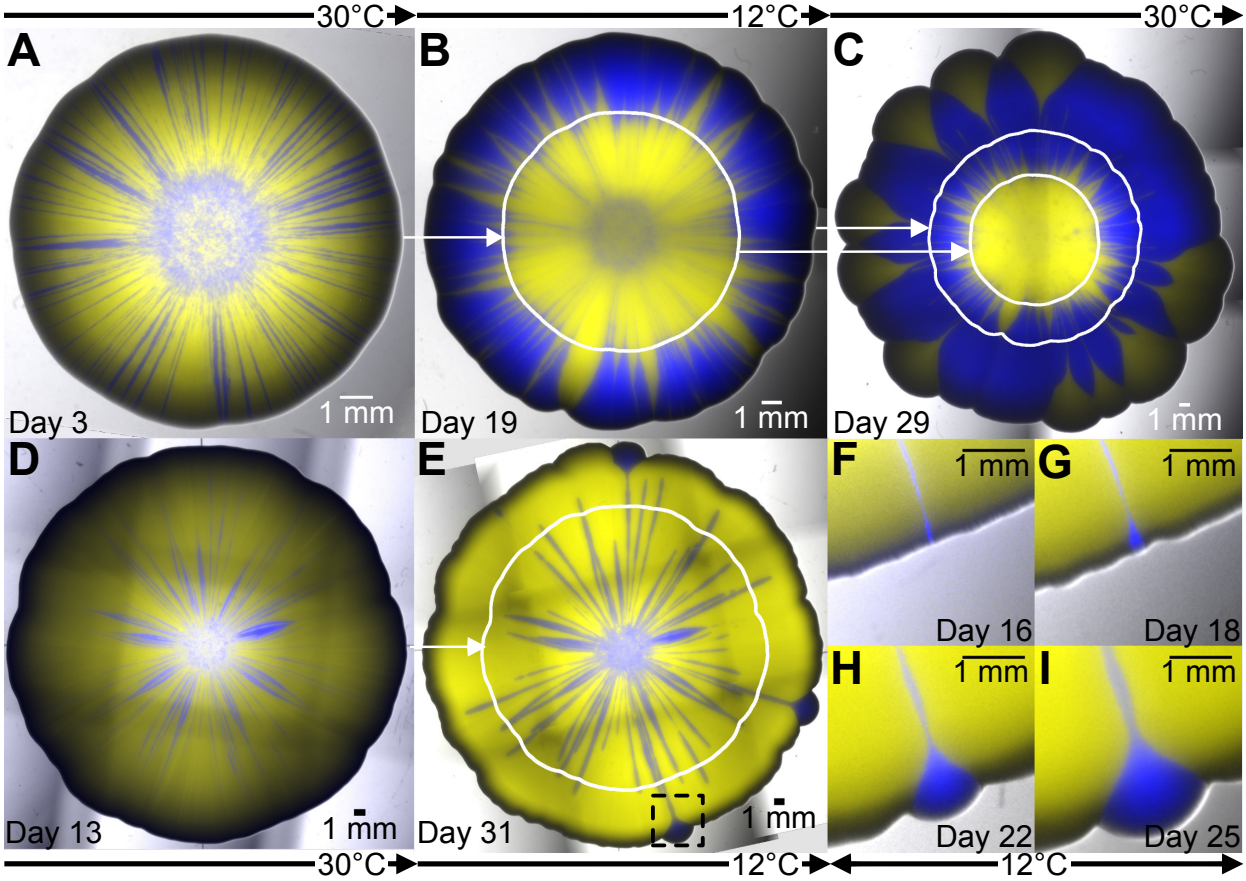

Fig. 2. Colony-growth experiments in time-varying environments highlight the relevance of mechanical interactions to the competition between strains growing in mixed colonies. (A) Mixed yAG1 (blue, 50% initial frequency, the faster-growing strain at 12˚C) and yAG2 (yellow, 50% initial frequency, the faster-growing strain at 30˚C) colony grown at 30˚C for 3 days. The colony was then grown for 16 days at 12˚C (B) and for further 10 days at 30˚C (C). (D) A different, mixed yAG1 (blue, 50% initial frequency) and yAG2 (yellow, 50% initial frequency) colony grown at 30˚C for 13 days. The colony was then grown for 18 days at 12˚C (E). At each temperature, the slower-growing strain survives as thin, persistent filaments that allow it to recover at the colony frontier following changes in temperature. White curves show the colony perimeter at the previous temperature switch. Pictures were taken immediately before temperature changes (A, B and D) and at the end of the experiments (C and E). Panels F-I show the recovery of the strain yAG1 (in the region corresponding to the black, dashed square in E) from a thin filament during growth at 12˚C. Differences in fluorescence intensity in panel C are due to the different height of the colony in the outer ring, which in turn is caused by the fact that the entire colony grows at 12˚C, but only the outer ring grows at 30˚C. Temperatures shown indicate the incubation temperature during the days immediately preceding the images. The colony sizes are rescaled to be approximately equal in radius.

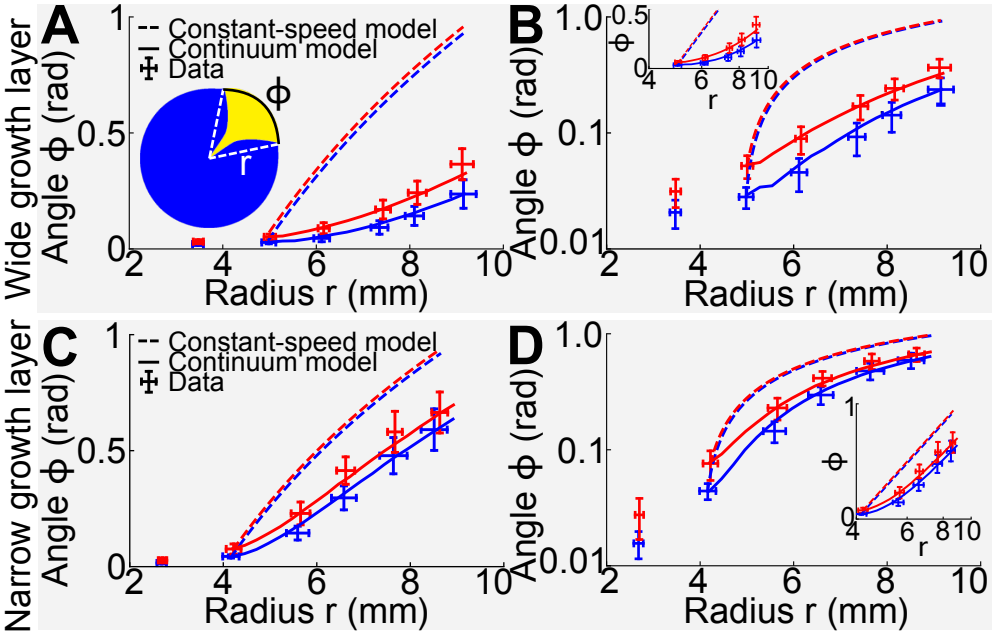

Fig. 3. Dynamics of sector opening angles (data points are mean±SD) of strain yAG2 opening into strain yAG1 at 30˚C after the inoculation of mixed-strain colonies with yAG2 relative frequency of 1%. The inset in (A) is a sketch of a sweeping sector within a colony. The radius r is defined as the distance from the center of the colony to the point at which the two strains meet at the frontier of the colony (dashed, white lines). The sector opening angle ϕ is the angle formed by the dashed, white lines, subtended by the arc shown in black. Experimental data were divided in two classes with equal numbers of sectors, based on the opening angle at the second measurement point (blue: small angle, red: large angle, SI Methods). Dashed curves are predictions of the constant-speed model. Continuous curves are best-fits to the continuum model. (A) Sector dynamics (red: 27 sectors, blue: 27 sectors) of the fitter strain in colonies with a wide layer of active growth at the frontier. (B) Same as panel A in log-linear scale. The inset shows the same data (with radii≥4 mm) in linear-log scale, where the constant-speed model prediction is a straight line. (C-D) Same as (A-B) for sector dynamics in colonies with a narrow layer of active growth at the frontier (red: 10 sectors, blue: 10 sectors). Experimental data show that opening angles increase more rapidly for narrow growth layers (C-D) than for wider ones (A-B). The transition between the exponential and logarithmic growth of opening angles with the radius r is clearly visible in (D). The constant-speed model (dashed lines) cannot reproduce the initial opening angles dynamics. The continuum model (continuous lines), on the other hand, can reproduce the data, using the growth layer width δ as a parameter. In (A-B), the best-fit parameter was δ=320 μm and in (C-D) it was δ=95 μm.

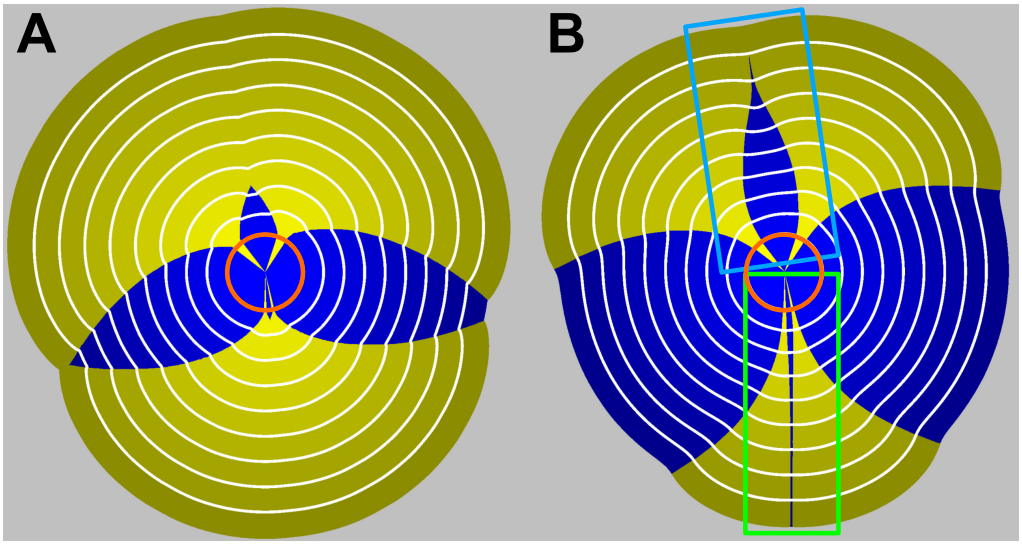

Fig. 4. The constant-speed model inspired by geometrical optics (A) and the continuum model (B) make different predictions for the competition of yeast strains in growing colonies. Both models were integrated numerically, starting from the same initial condition, corresponding to the (orange) contour in both panels. The constant-speed model (A) fails to reproduce the thin, persistent filaments observed experimentally (Fig. 1A-A2), but such a filament is seen for the blue strain in the continuum model (B, green rectangle). The opening angle of the yellow sectors increases faster in the constant-speed model (A) than in the continuum model (B), consistent with the experimental observations in Fig. 3. The survival of thin, persistent filaments in the continuum model depends on the angle at which sweeping sectors of the faster-growing strain meet at the edge of the colony. Faster-growing, yellow sectors whose boundaries are initially almost parallel to each other (corresponding to a small initial blue sector width, green rectangle) favor the survival of the slower-growing, blue sector for longer times than blue sectors trapped between yellow sectors whose boundaries collide with each other at substantial angles (light blue rectangle). White contours show the colony frontier at regularly-spaced time intervals. Different shades of yellow and blue show the strains' distribution in space at different times. The model parameters are representative of the experiments with a wide layer of active growth at the frontier: $\bar{v}_1$=1.89 mm/d, $\bar{v}_2$=2.33 mm/d (for both the constant-speed and the continuum model) and the growth layer width was set to the best-fit estimate δ=320 μm (continuum model). Pressure contours in the continuum model simulations are shown in Fig. S14.

Supplementary Information for

Physical interactions reduce the power of natural selection in growing yeast colonies

Andrea Giometto[1,2,3], David R Nelson[1,2,3,4], Andrew W Murray[2,3]

1. Department of Physics, Harvard University, Cambridge, Massachusetts, United States of America
2. FAS Center for Systems Biology, Harvard University, Cambridge, Massachusetts, United States of America
3. Department of Molecular and Cellular Biology, Harvard University, Cambridge, Massachusetts, United States of America
4. School of Engineering and Applied Sciences, Harvard University, Cambridge, Massachusetts, United States of America

This PDF file includes:

Table S1
Supplementary Methods
Supplementary Text
Figs. S1 to S14
Caption for movie S1
References for SI reference citations

Other supplementary materials for this manuscript include the following:

Movie S1

Table S1. Strain list

Name	Genotype
yAG1	*MATa BUD4-S288C can1-100 leu2Δ::prACT1-ymCitrine-tADH1-His3MX6 ura3Δ0*
yAG2	*MATa ade1-14 ADE2 bar1 BUD4-S288C can1-100 cyh2r his3-11 leu2 Δ ::HphMX4::ymCherry trp1-1 ura3-1*
yAG19	*MATa cin2Δ::LEU2 his3Δ200 leu2-3,112 prACT1::ymCherry-kanMX4 ura3-52*
yAG20	*MATa can1-100 cdc26Δ::URA3 his3-11,15 leu2-3,112 prACT1:ymCitrine-kanMX4 trp1-1 ura3-1*

All the strains, except yAG19, are in the W303 background and came from the Murray lab collection. The strain yAG19 is derived from S288c and was modified from strain DBY3391 (1).

Supplementary Methods

Sector opening angles. We identified sectors that were sufficiently far from each other on the last measurement time point (e.g., the four isolated sectors at 2, 8, 9 and 11 o' clock in Fig. 1A) of each mixed-strain colony and used these sectors to measure the temporal dynamics of sector opening angles. For each given colony and sector therein, we measured the opening angle at each available measurement time point. For the wide growth layer experiment, we measured the temporal dynamics of 54 sectors. For the narrow growth layer experiment, we measured the temporal dynamics of 20 sectors. To compare the model with the experimental data, we used the second available measurement time point as initial condition for the model (see SI section 6 for an explanation). We grouped sector opening angle trajectories (curves in Fig. S8) into two classes based on the opening angle of each sector at the second measurement point. The two classes were determined such that each class contained the same number of sector trajectories and were "small angles" (0.02-0.04 rad for the wide growth layer experiment and 0.030-0.052 rad for the narrow growth layer experiment) and "large angles" (0.04-0.10 rad for the wide growth layer experiment and 0.052-0.120 rad for the narrow growth layer experiment). To compute the best-fit parameter δ for the wide growth layer experiment, we simulated the continuum model varying the growth layer width δ between 250 μm and 450 μm, with 10 μm increments. The best-fit parameter was computed by maximizing the log-likelihood assuming Gaussian errors on the sector opening angles. Errors were computed as the minimum and maximum values of δ satisfying $\Delta(\ln L)=1/2$, where $(\ln L)$ is the log-likelihood. Fitting the small initial opening angle data (blue dots in Fig. 3A-B) and the large initial opening angle data (red dots in Fig. 3A-B) alone gives the best-fit estimates δ=350±50 μm (about 70 cell diameters) and δ=300±40 μm (about 60 cell diameters), respectively, which are both compatible with the estimate derived using the two data sets simultaneously. To compute the best-fit parameter δ for the narrow growth layer experiments, we simulated the continuum model varying the growth layer width δ between 70 μm and 130 μm, with 5 μm increments. Fitting the small initial opening angle data (blue dots in Fig. 3C-D) and the large initial opening angle data (red dots in Fig. 3C-D) alone gives the best-fit estimates δ=105±20 μm (about 21 cell diameters) and δ=85±15 μm (about 17 cell diameters), which are compatible with the estimate derived using both data sets simultaneously.

Continuum model. The expansion speed of a circular single-strain colony in the continuum-model can be computed as follows. The colony reproduces within a layer of width δ from the colony frontier. In a time-interval dt, the number of newborn cells in a circular colony of radius r is equal to $dN = \rho_{2d}\bar{g}dt\pi[r^2 - (r-\delta)^2] = \rho_{2d}\bar{g}dt\pi(2r\delta - \delta^2)$, where ρ_{2d} is the two-dimensional colony density (indicated by the symbol ρ in the main text). Because ρ_{2d} is assumed constant within the colony, we can imagine that newborn cells are, in effect, placed on a ring of radial extent dr at the outer-edge of the colony. Upon equating the number of cells contained in such a ring of width dr to the number of newborn cells dN, we find $\rho_{2d}\bar{g}dt\pi(2r\delta - \delta^2) \equiv \rho_{2d}\pi[(r+dr)^2 - r^2] = \rho_{2d}\pi(2rdr + dr^2)$. If we neglect the second-order term dr^2, we find the radial expansion velocity $\bar{v} = dr/dt = \bar{g}\delta[1 - \delta/(2r)] \cong \bar{g}\delta$, where the last approximation is justified because typically $\delta \ll r$ in colony-growth experiments. The continuum model was solved numerically using level-set methods (2). We wrote our implementation of the continuum model in the programming language Cython. Each strain's position in space was defined using a level-set function, i.e., a function that is negative within the domain occupied by a strain and positive outside. In our implementation of the model, the level-set function was the signed distance

function, i.e. the minimum signed distance between each point in space and the curve that identifies the spatial boundary of a strain. This signed distance function was computed at each temporal time step with the fast-marching method using the scikit-fmm Python extension module (https://github.com/scikit-fmm/scikit-fmm). The Poisson equation for the pressure field (Eq. 5) was solved numerically at each time step using the Jacobi iterative method. The Laplacian was computed using the D2Q9 stencil (3) for all the internal points within the colony, i.e., points at a distance larger than $\sqrt{2}h$ from the colony frontier, where h is the lattice spacing. For the points at the edge of the colony, i.e., the points at a distance smaller than $\sqrt{2}h$ from the colony frontier, we used the D2Q5 stencil modified as follows: at a given grid point, if one of the neighboring grid points crossed the frontier and was thus outside the colony, we modified the D2Q5 stencil by interpolating the position of the frontier along the vertical or horizontal coordinate (or both), and used the interpolated position in the given direction to compute the Laplacian. By doing so, the Laplacian was always evaluated using spatial coordinates at a signed distance $d \leq 0$ from the colony frontier. The velocity field $\vec{v}$ was computed numerically using the D2Q9 stencil for internal points and using the modified D2Q5 stencil for the points at the edge of the colony. The signed distance functions were propagated in time using Godunov's scheme (2). The accuracy of the numerical scheme was checked by simulating the growth of single-strain colonies and comparing the radial growth velocity to the analytical solution, and by simulating the growth of colonies composed of two strains with equal growth rate and checking that each strain's sectors maintained constant opening angles.

Constant-speed model. The constant-speed model (4) is inspired by geometrical optics and assumes that each strain expands at a constant speed (characteristic of the strain) perpendicular to the colony frontier. To compare the constant-speed model with the dynamics of opening angles (Fig. 3), we used the mean strain expansion velocities measured in single-strain colony growth experiments. We implemented the constant-speed model numerically using level-set methods, by modifying the code for our continuum model as follows. Instead of solving the Poisson Eq. 5 for the pressure field and computing the velocity field via Eq. 4, which are specific to the continuum model, we computed the velocity field within a narrow ring of width $4h$ (h is the lattice spacing) around the colony frontier, endowed it a velocity modulus of $\bar{v}_1$ or $\bar{v}_2$ depending on which strain occupied each location in space, and then assigned it the direction perpendicular to the colony frontier, towards the exterior of the colony.

Supplementary Text

1. The time to sector extinction depends on the angle formed by sectors of the faster-growing strain

Thin, persistent filaments can prolong the survival of the less-fit strain for long times in the growing layer of an expanding colony. Such filaments form when two sectors of the faster-growing strain are close to each other at the frontier of a colony and the lines perpendicular to each sector's outer boundary (i.e., the local directions of colony expansion) are almost parallel (e.g., the yellow sectors at the two sides of point 1 in Fig. S1A). If the boundaries between the faster- and slower-growing sectors are not parallel to each other (e.g., the yellow sectors at either side of point 2 in Fig. S1B), filaments persist for a much shorter time. This phenomenon leads to the surprising result that descendants of the blue strain close to point 1 in Fig. S1A last much longer than descendants of the blue strain close to points 2 and 3 in Fig. S1A. Fig. 4B shows that this phenomenon can be reproduced by the continuum model.

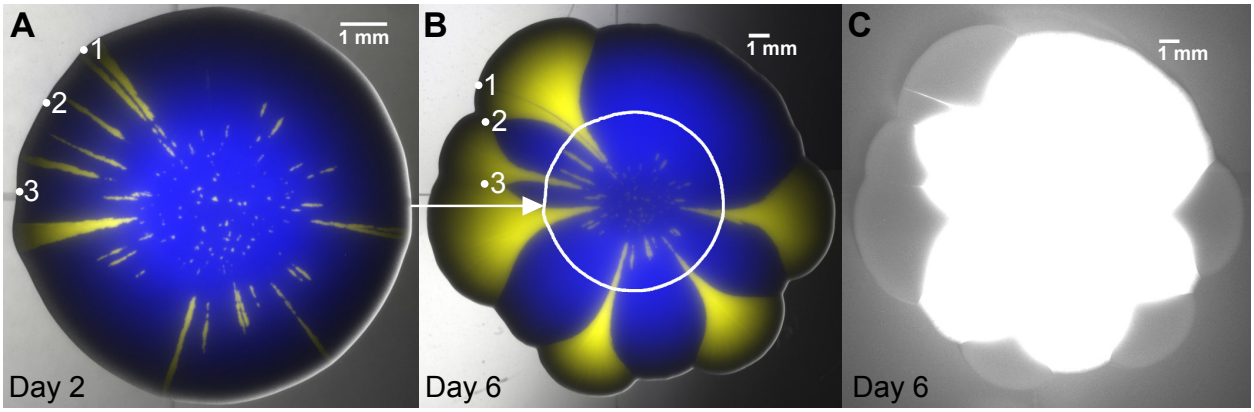

Fig. S1. The extinction time of sectors of the slower-growing strain (blue) depends on the angle at which sectors of the faster-growing strain meet at the frontier of a colony. (A) shows a mixed-strain colony grown at 30˚C for two days. The relative frequencies of strains yAG1 (blue) and yAG2 (yellow) in the inoculum were 99% and 1%, respectively. (B) shows the same colony after four further days of growth at 30˚C. The white curve in (B) shows the colony perimeter at day 2 (A). (C) shows the fluorescent channel corresponding to the strain yAG1 (blue) in (B), overexposed to show that the thin, persistent filament close to point 1 (B) is not extinct, while the originally wider filaments close to points 2 and 3 (B) are extinct. This experiment shows that descendants of the blue strain close to point 1 in (A) survived much longer than those of the blue strain next to points 2 and 3 (A), despite forming a sector that was much smaller than the blue sectors centered on points 2 and 3 after the first two days of growth (A).

2. Thin, persistent filaments can form without cell division

Fig. S2 shows that the heat-sensitive, *cdc26Δ*, strain yAG20 (magenta) does not expand spatially when grown at 37˚C (after a nine-hour lag time), while the strain yAG19 (cyan) does and thus forms expanding bulges at the boundary of mixed-strain colonies, displacing the heat-sensitive strain outwards. Thin, persistent filaments of the heat-sensitive strain yAG20 form between expanding yAG19 sectors (Fig. 1C-C1, main text), showing that physical interactions alone must be responsible for forming these filaments.

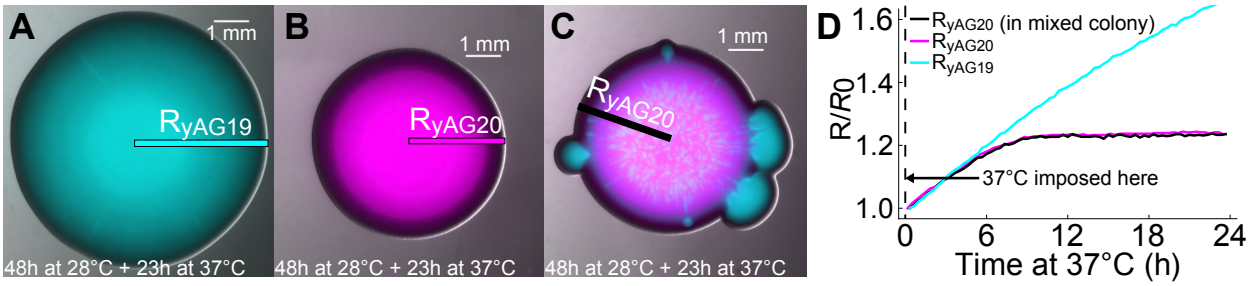

Fig. S2. The strain yAG20 (magenta) stops expanding when grown at 37˚C. (A-C) Combined fluorescent and bright-field images of single-strain yAG19 (cyan, A) and yAG20 (magenta, B) colonies and a mixed-strain yAG19 and yAG20 colony (C) after two days of growth at 28˚C and a further 23 h of growth at 37˚C (initial relative frequencies were 5% yAG19 and 95% yAG20). (D) Radius-vs-time curves of single-strain (cyan curve for yAG19 and magenta curve for yAG20) and mixed-strain (black curve for yAG20 within mixed colonies) colonies. Colonies were grown for two days at 28˚C before the start of the measurement, which was performed on a stereoscope incubated at 37˚C. After an approximately nine-hour lag, yAG20 (magenta) stopped growing. Radius-vs-time curves were measured by taking combined fluorescent and bright-field images of colonies (A-C) and fitting a circle to their perimeter. The black curve shows radii fitted to the perimeter of the strain yAG20 within the mixed-strain colonies, far from yAG19 sectors (C). Note that the black curve is almost indistinguishable from the magenta curve obtained for yAG20 grown in isolation.

3. Thin, persistent filaments dynamics

The fact that persistent filaments are thin (about 150 μm or 30 cell diameters) might suggest that their dynamics should be strongly influenced by the stochasticity of cell division. Visual inspection of their spatial and temporal dynamics, however, shows that the strain boundaries on either side of such filaments follow smooth trajectories in space (Fig. 1A and Fig. S1B are typical examples). Relative fluctuations of the filament thickness in the direction orthogonal to the filament long axis are less than 10% (Fig. S3B). In one of our experiments, we could visualize a lineage trajectory within a thin, persistent filament, giving us a more detailed view of its dynamics. We could visualize the lineage because a cell of the strain yAG2 located at the start of a filament (point *O* in Fig. S3B), and its descendants, showed increased fluorescence intensity compared to other yAG2 cells. The smoothness of the lineage trajectory (high grayscale intensity in Fig. S3B-C) further suggests that the dynamics of thin, persistent filaments is more deterministic than one might expect from the fact that filaments are only about 30 cells wide. The lower-than-expected stochasticity of filament boundaries is likely due to the fact that actively-dividing cells form a layer of about 300-600 μm from the colony frontier (section 5 and Fig. S7), and thus the number of dividing cells within a 150 μm-wide filament is about 150 μm × 450 μm / 5 μm≈10^4 cells (5 μm is the typical

cell diameter), assuming that the colony is a monolayer. Because yeast colonies are not monolayers and are about 30 μm-high (6 cell diameters) within 500 μm from the outer frontier, the number of dividing cells is even larger. Thus, the dynamics of thin, persistent filaments is determined by the cell division dynamics of more than 10^4 cells, and not the 30 cells at the frontier alone, thus reducing its stochasticity.

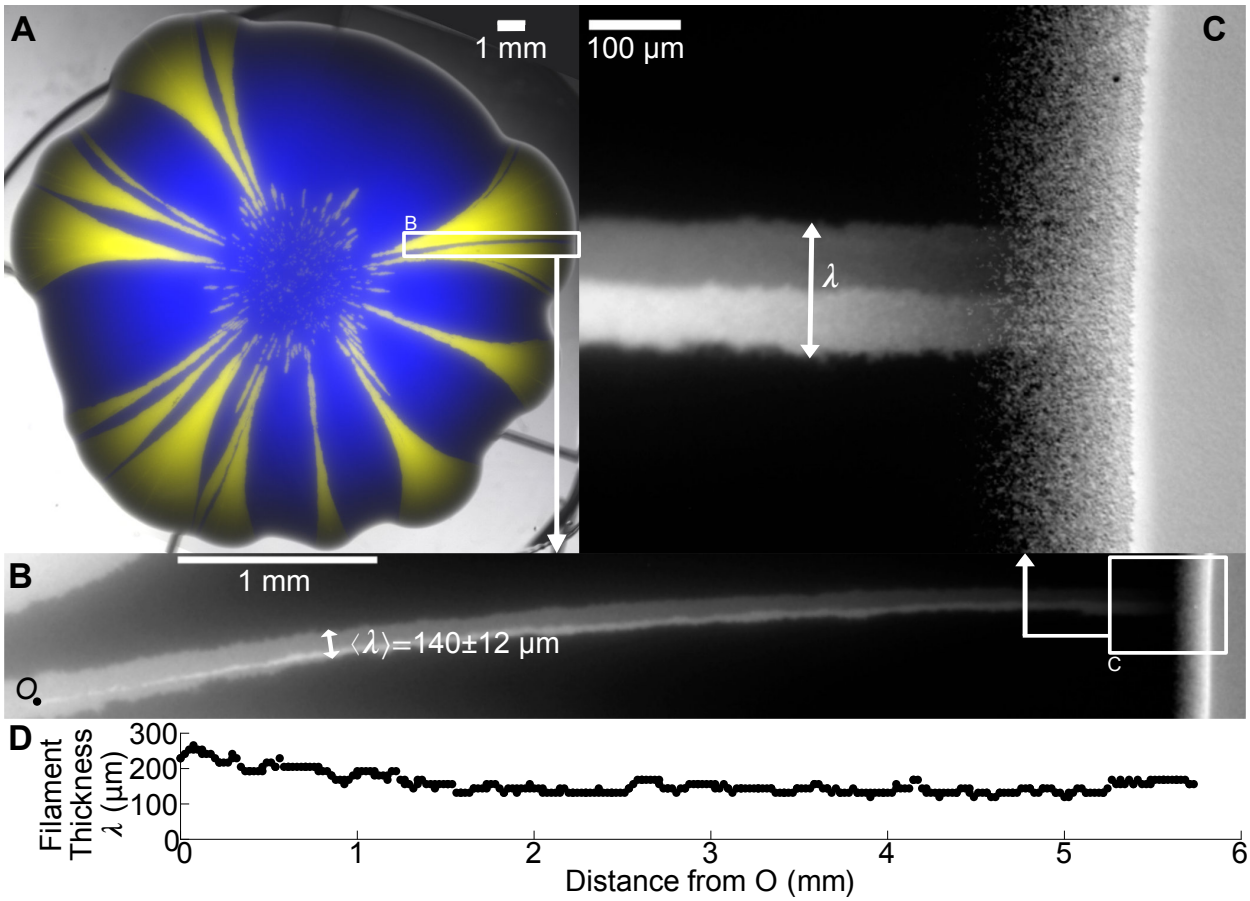

Fig. S3. Fluctuations of thin, persistent filament boundaries and lineage dynamics within a filament. Panel A shows a combined fluorescent and bright-field image of a mixed-strain colony grown for four days at 30°C (initial relative frequencies were 99% yAG1, blue, and 1% yAG2, yellow). Panels B and C show the fluorescent channel corresponding to the strain yAG2 (blue in A), combined with the bright-field channel. Within one of the persistent filaments in this colony (B), a cell (at point *O*) and its descendants showed increased fluorescence intensity compared to other yAG2 cells, allowing us to observe a lineage within the filament. Panel C shows the filament close to the colony frontier. Because the bright-field signal is inversely proportional to the colony height, individual cells can be seen at the colony frontier, where the colony is a single cell layer. On the left of panel C, instead, the grayscale image is dominated by the fluorescent signal, which is proportional to the colony height. Panel D shows the thickness λ of the filament in the direction orthogonal to the filament's long axis, at different distances from the point *O* along the filament's long axis. The filament thickness decreases very slowly and reaches an almost constant value of $\langle\lambda\rangle$=140±12 μm wide (mean±SD) at distances larger than 2 mm from point *O* along the filament long axis. Thus, fluctuations of the filament thickness are only 9% (CV=SD/mean) of the filament

average thickness $\langle\lambda\rangle$. Filament boundaries were computed using the EdgeDetect routine of the software Wolfram Mathematica, version 11.

4. Experiments in time-varying environments

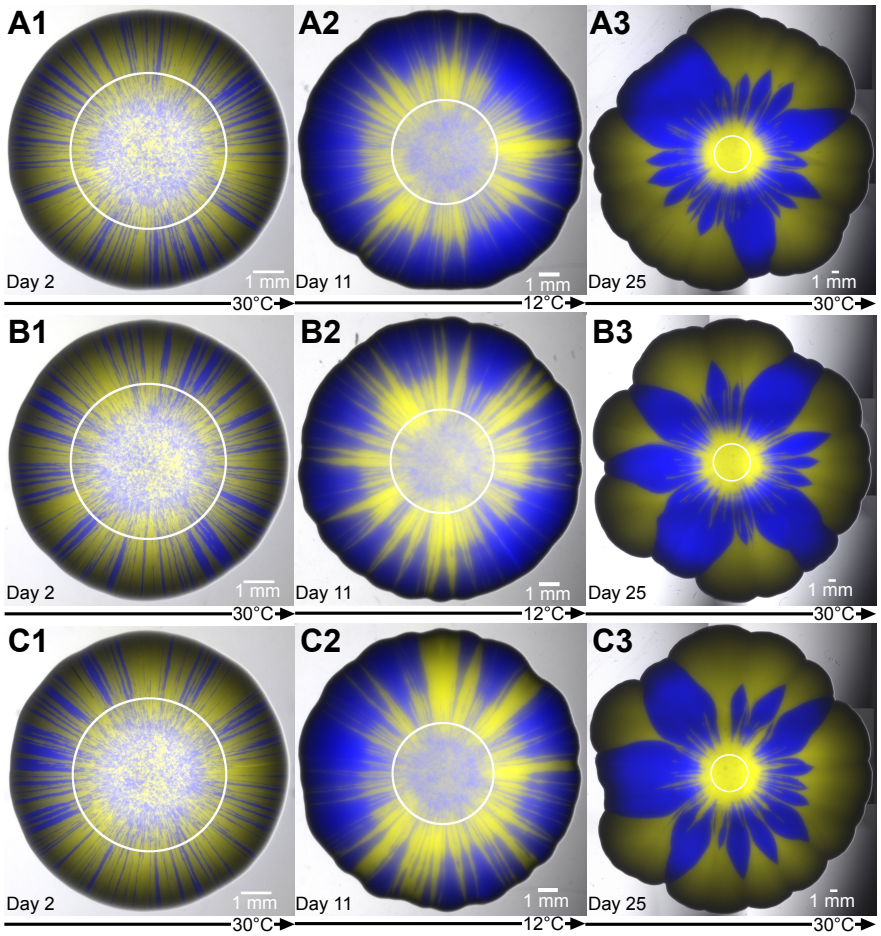

Fig. S4. Three replicates of mixed colony-growth in temporally-varying environments. Panels A1, B1 and C1 show mixed yAG1 (blue, 50% initial frequency) and yAG2 (yellow, 50% initial frequency) colonies grown at 30˚C for 2 days. The colonies were then grown for 9 days at 12˚C (panels A2, B2 and C2) and for further 14 days at 30˚C (panels A3, B3 and C3). At each temperature, the slower-growing strain survives as thin, persistent filaments that allow it to recover at the colony frontier following a temperature change that gives it a selective advantage. Pictures were taken immediately before temperature changes (A1, A2, B1, B2, C1 and C2) and at the end of the experiments (A3, B3 and C3). The relative orientation of the colonies may vary slightly along rows. Solid white circles with diameter 5 mm are shown as references, as a reminder that the overall colony sizes are increasing from left to right. Temperatures shown indicate the incubation temperature during the days immediately preceding the images.

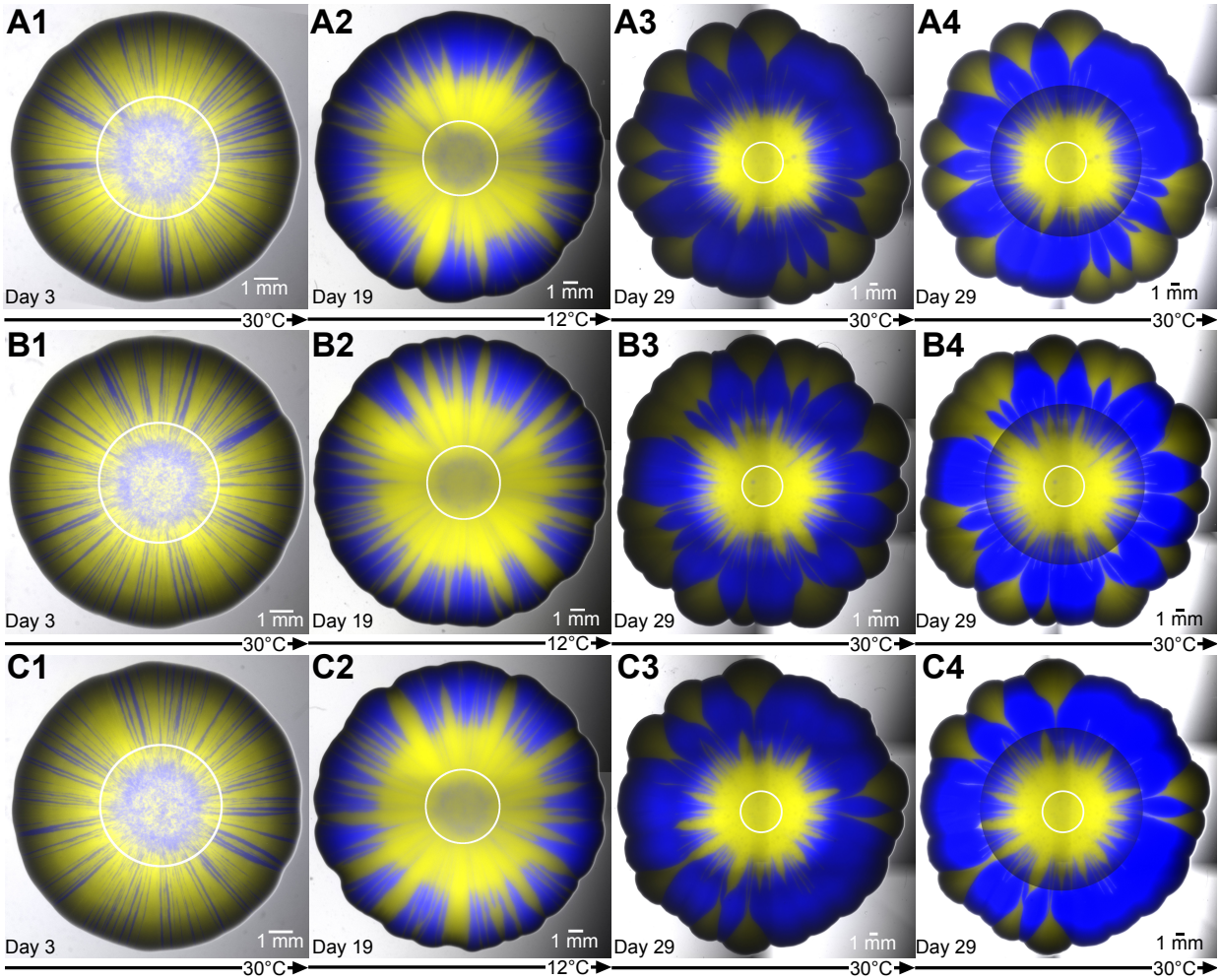

Fig. S5. Three replicates of mixed colony-growth experiments in temporally-varying environments. This experiment uses a different time series of environments than the experiment shown in Fig. S4. Panels A1, B1 and C1 show mixed yAG1 (blue, 50% initial frequency) and yAG2 (yellow, 50% initial frequency) colonies grown at 30˚C for 3 days. The colonies were then grown for 16 days at 12˚C (panels A2, B2 and C2) and for further 10 days at 30˚C (panels A3, B3 and C3). To highlight the recovery of yAG2 in the last environmental phase, panels A4, B4 and C4 show the same images as panels A3, B3 and C3, with brightness and contrast enhanced in the outer ring. Panels A1-A4 show the same colony as the one shown in Fig. 2A-C. At each temperature, the slower-growing strain survives as thin, persistent filaments that allow it to recover at the colony frontier following a temperature change that gives it a selective advantage. Pictures were taken immediately before temperature changes (A1, A2, B1, B2, C1 and C2) and at the end of the experiments (A3, B3 and C3). The relative orientation of the colonies may vary slightly along rows. White circles with diameter 5 mm are shown as references, as a reminder that the overall colony sizes are increasing from left to right. Temperatures shown indicate the incubation temperature during the days immediately preceding the images.

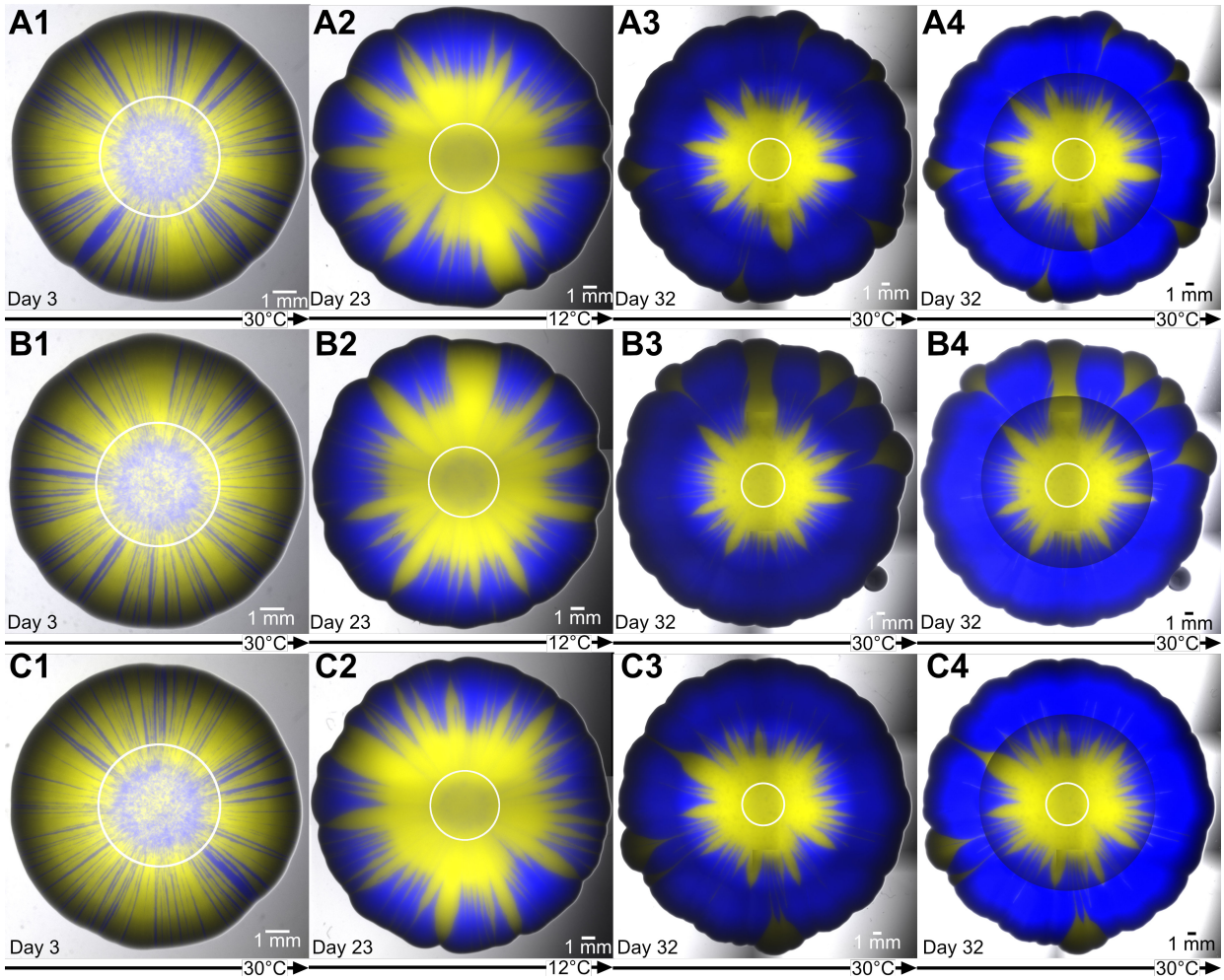

Fig. S6. Three replicates of mixed colony-growth experiments in temporally-varying environments. This experiment uses a different time series of environments than the experiments shown in Fig. S4 and Fig. S5. Panels A1, B1 and C1 show mixed yAG1 (blue, 50% initial frequency) and yAG2 (yellow, 50% initial frequency) colonies grown at 30˚C for 3 days. The colonies were then grown for 20 days at 12˚C (panels A2, B2 and C2) and for further 10 days at 30˚C (panels A3, B3 and C3). Differences in fluorescence intensity in panels A3, B3 and C3 are due to the different height of the colony in the outer ring, which in turn is caused by the fact that the entire colony grows at 12˚C, but only the outer ring grows at 30˚C. To highlight the recovery of yAG2 in the last environmental phase, panels A4, B4 and C4 show the same images as panels A3, B3 and C3, with brightness and contrast enhanced in the outer ring. At each temperature, the slower-growing strain survives as thin, persistent filaments that allow it to recover at the colony frontier following a temperature change that gives it a selective advantage. Pictures were taken immediately before temperature changes (A1, A2, B1, B2, C1 and C2) and at the end of the experiments (A3, A4, B3, B4, C3 and C4). The relative orientation of the colonies may vary slightly along rows. White circles with diameter 5 mm are shown as references, as a reminder that the overall colony sizes are increasing from left to right. Temperatures shown indicate the incubation temperature during the days immediately preceding the images. The gray disk in the lower-right corner of panels B3 and B4 is a contamination.

5. Growth layer width

We measured the growth layer width in colony-growth experiments by following the fate of thin sectors that were extinguished by genetic drift. We recorded time-lapses of mixed-strain, growing colonies, taking fluorescent and bright-field images every 30 min. Occasionally, sectors of the faster-growing strain yAG2 went extinct and thus failed to sweep. For every such sector, we measured its length L and the distance d of its tip from the edge of the colony (Fig. S7A-C). Plotting L vs time (Fig. S7D) identified the time point at which these sectors stopped expanding appreciably (e.g., point B in Fig. S7D). We took the distance d from the tip of the sector to the edge of the colony at this time point as our estimate of the growth layer width. Fig. S7E shows summary statistics of such measurements performed across multiple sectors that went extinct. We measured the growth layer width of colonies grown on 35 mm, 7 mL YPD 1% agarose discs surrounded by liquid YPD medium which was substituted daily ("wide" treatment in Fig. S7E) and the growth layer width of colonies grown on 100 mm, 33 mL YPD 1% agarose plates, in the absence of liquid YPD medium ("narrow" treatment in Fig. S7E). The growth layer width was larger in the first set of experiments (mean=530 μm, SD=120 μm) than in the second (mean=340 μm, SD=90 μm), two-sample *t*-test(*d.f.*=28)=5.165, $p<10^{-4}$. Note that these estimates of the growth layer width are larger than the best-fit values of the growth layer width δ in the continuum model. This discrepancy is not surprising, for two reasons: *i)* for simplicity, the continuum model assumes that the growth function goes to zero discontinuously at a distance δ from the colony frontier, while the cell division rate in the experiments is likely a continuous function of the distance from the colony frontier; *ii)* the model assumes that the height of the colony is constant throughout the colony, whereas the height of the experimental colonies is reduced at the frontier. In fact, if we consider an experimental, circular colony of radius r on top of an agar plate in the plane (x, y) with center in $(x, y) = (0,0)$, the three-dimensional profile of the colony in the plane (x, z) along the axis $y = 0$ is approximately triangular at the frontier ($x \simeq r$). The colony height goes from $h = 0$ μm at $x = r$, to $h \simeq 30$ μm at $x = r - \delta_{exp}$, where δ_{exp} is the growth layer width estimated experimentally. The model, instead, assumes that the colony has a rectangular profile at the frontier in the (x, z) plane (i.e., constant $h = 30$ μm in $r - \delta_{model} \leq x \leq r$). Equating the total number of cells in the experimental growth layer (per unit width in the direction orthogonal to the colony frontier), $\rho\delta_{exp}h/2$ (ρ is the three-dimensional cell density), to the total number of cells in the continuum-model growth layer (per unit width in the direction orthogonal to the colony frontier), $\rho\delta_{model}h$, gives $\delta_{exp} = 2\delta_{model}$. Observations *i)* and *ii)* above suggest that the best-fit parameter of δ in the continuum-model should thus be smaller than the length-scale measured in the experiments.

We attribute the difference in growth layer widths between the two experimental settings (wetter and drier plates) to differences in the height of the colonies relative to the surface of the agar in the two setups. Colonies grow less tall on YPD agarose discs surrounded by liquid YPD medium (wide growth layer) than on standard YPD agar plates (narrow growth layer). Assuming that, at steady state, nutrients are depleted below the colony and that the nutrient flux from the exterior of the colony sustains the same, constant number of actively-growing cells at the colony frontier, the width of the actively growing layer should decrease as the colony height increases, as we observed experimentally. The following back-of-the-envelope calculation suggests that colony height and growth layer widths should be inversely proportional to each other, all other parameters being equal. Considering for simplicity a single-strain colony with radius r much larger than the width

of the growth layer δ at the colony frontier, the total number of cells in the colony increases by $dN = (2\pi r\rho h\bar{v})dt = (2\pi r\rho h\bar{g}\delta)dt$ in a time dt, where ρ is the three-dimensional colony density, h is the height of the colony, $\bar{g}$ is the (constant) growth rate within the actively reproducing layer and we have used the fact that $\bar{v} \cong \bar{g}\delta$. Upon assuming that the growth rate $\bar{g}$, the three-dimensional density ρ and the total number of newborn cells per unit time dN/dt (at the same radius r) do not vary between the experiments, one finds that the product $h\delta$ should also be constant, i.e., the height of the colony should be inversely proportional to the growth layer width. Even though the assumptions made in this simple calculation may not be satisfied exactly in our experimental settings, this calculation offers physical intuition for the factors controlling the width of the actively growing layer. For the purpose of our investigation, it suffices to know that the difference in growth layer widths was measured experimentally (Fig. S7).

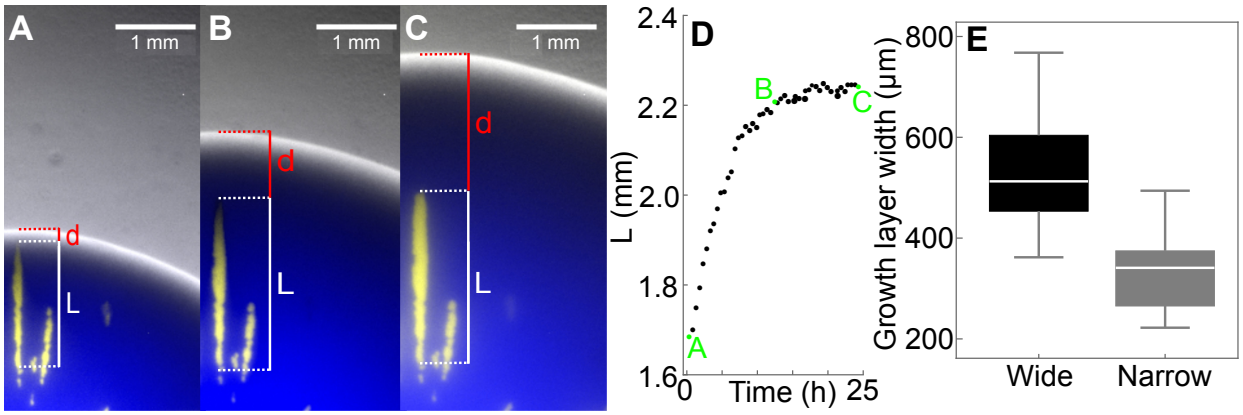

Fig. S7. (A-C) Combined fluorescent and bright-field images of yAG2 (yellow) sectors that went extinct despite their faster growth rate. The length L of such sectors and the distance d of the sector's tip from the edge of the colony were used to estimate the growth layer width in colony-growth experiments. (D) Length of the yellow sector shown in (A-C) at different times during a time-lapse acquisition. The growth layer width was measured as the value of d at the time when the sector's length L stopped growing appreciably (e.g., point B in panel D). Points A, B and C in panel D correspond to the images shown in panels A, B and C. (E) Box-whisker charts of measured growth layer widths in colony-growth experiments performed with different experimental setups. "Wide" refers to colonies grown on 35 mm, 7 mL YPD 1% agarose discs surrounded by liquid YPD medium which was substituted daily (as in the wide growth layer experiment). "Narrow" refers to colonies grown on 100 mm, 33 mL YPD 1% agarose plates, in the absence of liquid YPD medium (as in the narrow growth layer experiment). The growth layer width was larger in the first set of experiments (mean=530 μm, SD=120 μm) than in the second (mean=340 μm, SD=90 μm), two-sample *t*-test value(*d.f.*=28)=5.165, $p<10^{-4}$. The white horizontal lines in (E) are the median widths measured in 17 ("wide") and 13 ("narrow") yAG2 sectors that went extinct in 4 ("wide") and 6 ("narrow") colony-growth experiments, the boxes are the 25% and 75% quantiles and the edges of the whiskers are the minimum and maximum values within each class.

6. Initial condition for the model simulations

To compare the model for how the opening angle of sectors increased over time with the experimental data, we used the opening angle at the time point after the time point at which the sector was first detected as the initial condition for the model. We used the angle at the second time point for three reasons: *i)* the relationship between the initial opening angle and the final opening angle is much more variable if the initial opening angle is taken at the first measurement time point (Fig. S8A), compared to the second one (Fig. S8B); *ii)* when they are first detected, sectors subtend arcs that are only from 3 to 8 pixels in the fluorescent images of the colonies, and thus error in estimating their size is large; *iii)* simulating the dynamics of opening angles at the initial measurement time point in the continuum model requires a very fine resolution that we couldn't achieve with the available code and computational capabilities. Points *i)* and *ii)* are likely related.

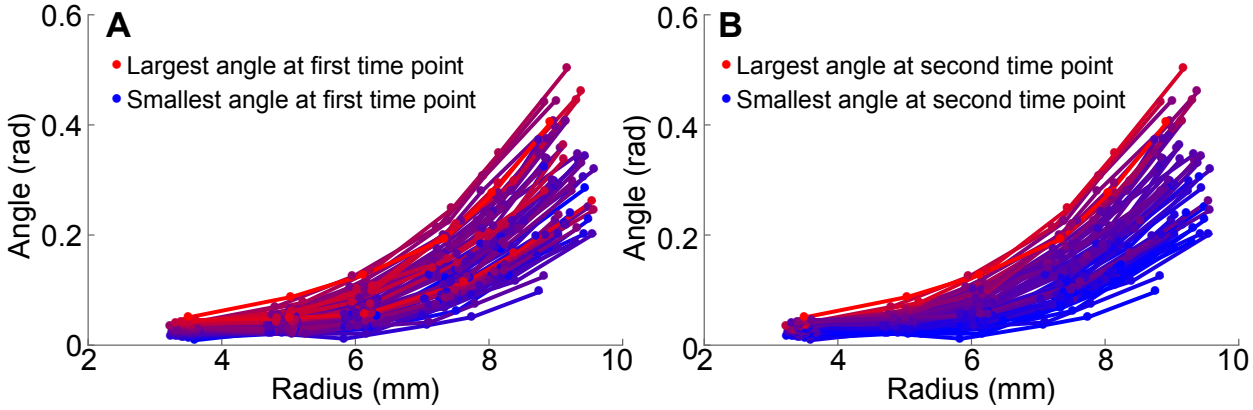

Fig. S8. Opening angle dynamics of sweeping yAG2 sectors (wide growth layer treatment, data used to generate Fig. 3A-B). (A) Dynamics of individual sector opening angles, color-coded according to the opening angle at the first time point from blue (smallest angle) to red (largest angle). (B) Dynamics of individual sector opening angles, color-coded according to the opening angle at the second time point from blue (smallest angle) to red (largest angle). The relationship between the initial and the final opening angle is more variable in (A), where the initial angle is taken at the first measurement time point. The increased variability compared to (B), where the angle for the color-coding is taken at the second measurement time point, is due to a combination of *i)* the dynamics being more variable when sector opening angles are small and *ii)* errors in the measurement of opening angles at the first measurement time point, when sectors subtend arcs that extend for only 3 to 8 pixels in the raw data images. The second measurement point was thus used as initial condition for the numerical integration of the continuum model in Fig. 3.

7. Single-strain expansion velocities during colony growth

Fig. S9 reports radii measurements performed on single-strain colonies in the wide and narrow growth layer experiments, and the expansion velocities computed from such data. These velocities were used for the comparison of opening angles dynamics between the experiments and the two models. The increase of mean radii with time is fit reasonably well by a straight line (Fig. S9A and C). Note that, however, mean expansion velocities computed as the difference between radii at consecutive times, divided by the corresponding time difference, decrease with time (Fig. S9B and D). This decrease is more pronounced for the narrow growth layer experiment (Fig. S9D) than for the wide growth layer experiment (Fig. S9B), and is frequently found in range expansion experiments over multiple days (4). In the wide growth layer experiment, in contrast with the narrow growth layer experiment, nutrients are replenished daily and the agar is always in contact with liquid medium. Thus, we attribute the increased reduction of the expansion velocity in the narrow growth layer experiment to the depletion of nutrients and the visible drying of agar plates with time. Nonetheless, because *i)* a linear fit of the radius-vs-time points is reasonably good for both experiments (Fig. S9A and C), *ii)* because the ratio between the two strains' expansion velocities is reasonably constant with time (insets of Fig. S9B and D), and *iii)* to keep the models simple, we considered temporally-constant velocities in both the constant-speed and the continuum models.

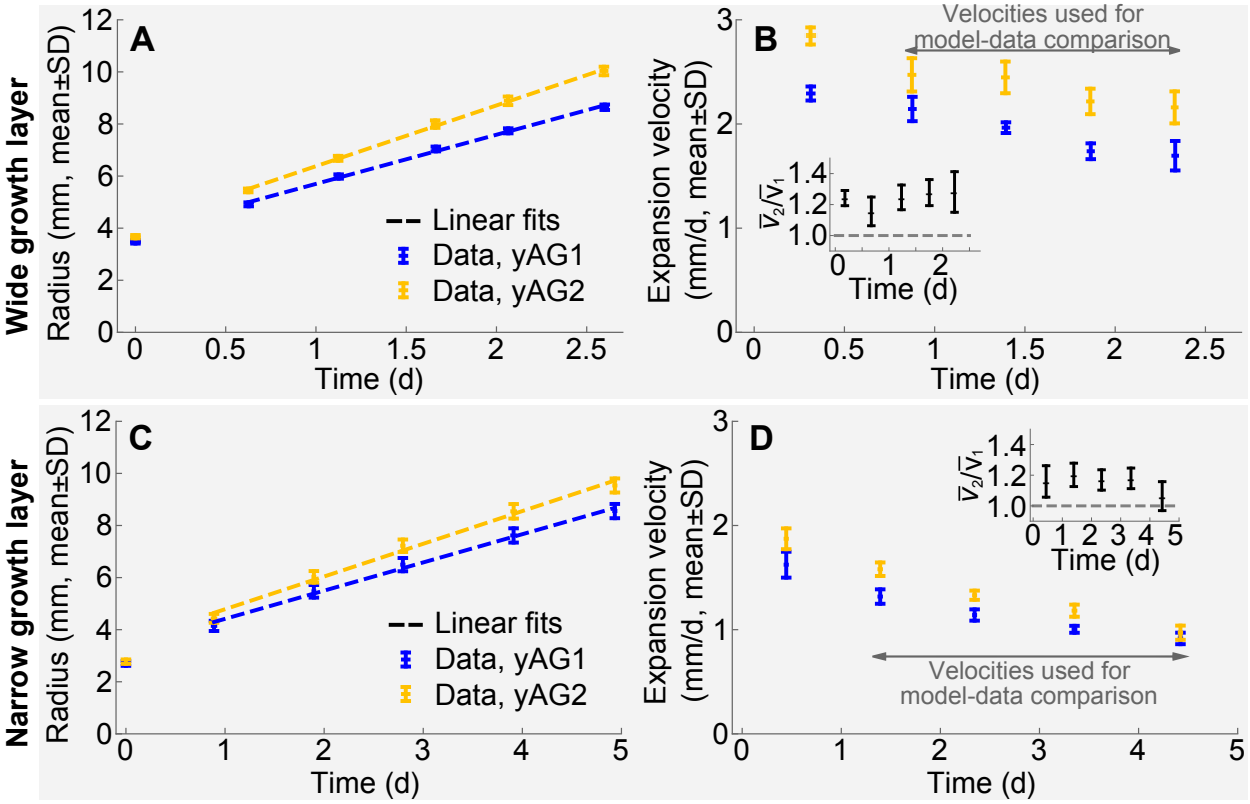

Fig. S9. Radii and velocities of single-strain colonies growing on agar discs surrounded by liquid medium (wide growth layer) or normal agar plates (narrow growth layer). (A) Mean radii of 10 single-strain yAG1 (blue) and 9 single-strain yAG2 (yellow) colonies at different times, measured in the wide growth layer experiment. Dashed lines show the best linear fits of the two strains' radii vs time, starting from the second measurement time point. (B) Expansion velocities computed as the differences of consecutive radii shown in (A), divided by the time-interval between such points. The inset shows the ratio between the two strains' expansion velocities at different times (mean±SD). (C) Mean radii of 11 single-strain yAG1 (blue) and 11 single-strain yAG2 (yellow) colonies at different times, measured in the narrow growth layer experiment. Dashed lines show the best linear fits of the two strains' radii vs time points, starting from the second measurement time point. (D) shows the expansion velocities computed as the differences of consecutive radii shown in (C), divided by the time-interval between such points. The inset in (D) shows the ratio between the two strains' expansion velocities at different times (mean±SD). Because we used the second time point as the starting point for the comparison of opening angles dynamics between models and experiments (see previous section, Fig. 3 and Fig. S8), expansion velocities were computed from the second time-point onwards. Time 0 is the first measurement time point (not the inoculation time). Velocity error bars are the standard deviations of the set of velocities calculated separately for each replicate colony expansion.

8. Derivation of the 2d model from the 3d Navier-Stokes equations

We consider a single-strain colony growing on the surface of an agarose plate. The continuity equation for the growing colony is:

$$\frac{\partial \rho}{\partial t} + \vec{\nabla} \cdot (\rho \vec{v}) = \rho g, \tag{S1}$$

where $\rho(x, y, z, t)$ is the three-dimensional (3d) density of the colony, $\vec{v}(x, y, z, t)$ is the velocity field within the colony, $\vec{\nabla}$ is the gradient operator and $g(x, y, z, t)$ is the position-dependent growth rate, which appears as a source term. Note that the symbols ρ, g, $\vec{v}$ (and p introduced in Eq. S4) in this section refer to 3d quantities and are not identical to the same symbols used in the main text (the mutual relationships are clarified at the end of this section). Let (x, y) be the plane of the plate and z the direction orthogonal to it. We assume that the density ρ is constant within the colony, i.e.:

$$\frac{D\rho}{Dt} \equiv \left(\frac{\partial}{\partial t} + \vec{v} \cdot \vec{\nabla}\right)\rho = 0, \tag{S2}$$

where $D\rho/Dt$ is the density's material derivative, which gives the temporal rate of change of ρ for a fixed material element moving with velocity $\vec{v}$. Upon combining the two equations, one has:

$$\vec{\nabla} \cdot \vec{v} = g, \tag{S3}$$

i.e., the 3d divergence of the velocity field is equal to the growth function g. The 3d Navier-Stokes equations describing the colony are:

$$\rho\left[\frac{\partial \vec{v}}{\partial t} + (\vec{v} \cdot \vec{\nabla})\vec{v}\right] = \mu \nabla^2 \vec{v} - \vec{\nabla} p = 0, \tag{S4}$$

where ∇^2 is the Laplacian operator, μ is the dynamic viscosity of the colony and $p(x, y, z, t)$ is the 3d pressure field within the colony. The last equality in Eq. S4 holds because inertial terms can be neglected for this system. Thus, Eq. S4 reduces to:

$$\mu \nabla^2 \vec{v} = \vec{\nabla} p. \tag{S5}$$

Let $h(x, y, t)$ be the height of the colony and $\vec{v} = (u, v, w)$ be the x, y, z components of $\vec{v}$. The boundary conditions are:

$$\vec{v}|_{z=0} = 0, \tag{S6}$$

$$\left.\frac{\partial u}{\partial z}\right|_{z=h} = \left.\frac{\partial v}{\partial z}\right|_{z=h} = 0, \tag{S7}$$

$$p(\vec{x}, \mathrm{t}) = p_0 \text{ for } \vec{x} \in \partial\Omega, \tag{S8}$$

where Eq. S6 is the no-slip boundary condition at the agar surface, Eq. S7 states that there is no tangential stress at the colony surface and Eq. S8 states that the pressure at the external boundary of the colony ($\partial\Omega$) is equal to the atmospheric pressure p_0. The notation $f|_{z=a}$, where f is a function of (x, y, z, t), denotes the evaluation at $z = a$. The no-slip boundary condition can be generalized to a slip boundary condition with similar results, as we show at the end of this section. We applied a centrifugal acceleration to experimental colonies to get an intuition for the appropriate boundary condition at the agar surface. No measurable displacement of the bottom

layer of the colony was observed, indicating that the no-slip condition is appropriate (Fig. S10), at least on time scales when the colony is not actively growing.

To derive the two-dimensional model for colony growth used in the main text, we average Eqs. S3 and S5 in the z-direction by integrating from $z = 0$ to $z = h$ and dividing by the colony height h. Eq. S3 becomes:

$$\frac{\partial \langle u \rangle_z}{\partial x} + \frac{\partial \langle v \rangle_z}{\partial y} + \frac{\mathrm{w}|_{z=h}}{h} = \langle g \rangle_z, \tag{S9}$$

where the symbol $\langle f \rangle_z$, with f a function of (x, y, z, t), denotes the average in the z-direction, i.e. $\langle f \rangle_z = h^{-1} \int_0^h dz\, f$. The surface of the colony is described by the equation $f(x, y, z, t) = h(x, y, t) - z = 0$. The material derivative of f is equal to zero at the surface, that is:

$$\begin{aligned} \left.\frac{Df}{Dt}\right|_{z=h} &= \frac{\partial f}{\partial t} + \mathrm{u}|_{z=h} \frac{\partial f}{\partial x} + \mathrm{v}|_{z=h} \frac{\partial f}{\partial y} + \mathrm{w}|_{z=h} \frac{\partial f}{\partial z} \\ &= \frac{\partial h}{\partial t} + \mathrm{u}|_{z=h} \frac{\partial h}{\partial x} + \mathrm{v}|_{z=h} \frac{\partial h}{\partial y} - \mathrm{w}|_{z=h} = 0, \end{aligned} \tag{S10}$$

which gives us an expression for $\mathrm{w}|_{z=h}$:

$$w|_{z=h} = \left(\frac{\partial}{\partial t} + \vec{v}|_{z=h} \cdot \vec{\nabla} \right) h = \left.\frac{D}{Dt}\right|_{z=h} h, \tag{S11}$$

which holds because h does not depend on z.

Assumption 1: we assume that the colony has constant height h, i.e. $D/Dt|_{z=h} h = 0$, given that experimental colonies are approximately flat in the direction parallel to the agar surface close to the frontier. Thus, from Eq. S11 we have $w|_{z=h} = 0$ and we get the 2d version of Eq. S9 :

$$\vec{\nabla}_{2d} \cdot \vec{v}_{2d} = \langle g \rangle_z, \tag{S12}$$

where $\vec{v}_{2d} = (\langle u \rangle_z, \langle v \rangle_z)$ is the 2d velocity given by the 3d velocity components u and v averaged in the z-direction and $\vec{\nabla}_{2d} = (\partial/\partial x, \partial/\partial y)$ is the 2d gradient in the plane (x, y). Eq. S12 is the 2d incompressibility condition used in the main text (Eq. 2 of the main text), where we dropped the angle brackets and subscript on $\langle g \rangle_z$ and the subscript on $\vec{v}_{2d}$ for simplicity, as all functions mentioned in the main text are 2d functions of x and y.

Assumption 2: we adopt a version of the lubrication approximation (24) to express Eq. S5 in terms of the (u, v) components of the velocity field, averaged in the z-direction. Let us consider the first component of Eq. S5:

$$\mu \nabla^2 u = \frac{\partial p}{\partial x}. \tag{S13}$$

Let U be the asymptotic (i.e., for colony radii $r \gg \delta$, where δ is the growth layer width) radial expansion rate of the yeast colony in the (x, y) plane. We can estimate the relative magnitude of the terms in $\nabla^2 u$ as:

$$\frac{\partial^2 u}{\partial x^2} + \frac{\partial^2 u}{\partial y^2} \sim \frac{U}{\delta^2}, \tag{S14}$$

$$\frac{\partial^2 u}{\partial z^2} \sim \frac{U}{h^2}, \tag{S15}$$

where the symbol $\sim$ indicates the order of magnitude. Because $\delta \gg h$ for growing yeast colonies (δ is about 300-600 μm, h is about 30 μm within 500 μm from the outer frontier of the colony in the (x, y) plane), the term $\partial^2 u/\partial z^2$ dominates over $\partial^2 u/\partial x^2 + \partial^2 u/\partial y^2$ and we can approximate Eq. S13 with:

$$\mu \frac{\partial^2 u}{\partial z^2} = \frac{\partial p}{\partial x}, \tag{S16}$$

which integrated in z gives, using the boundary condition in Eqs. S6 and S7:

$$u(x, y, z, t) = \frac{1}{\mu}\frac{\partial}{\partial x}\left[-z\int_0^h dz' p(x, y, z', t) + \int_0^z dz' \int_0^{z'} dz''\, p(x, y, z'', t)\right]. \tag{S17}$$

Dividing Eq. S17 by h and integrating in z from 0 to h, we find:

$$\langle u\rangle_z(x, y, t) = -\frac{h^2}{2\mu}\frac{\partial\langle p\rangle_z}{\partial x}(x, y, t) + \frac{1}{\mu h}\frac{\partial}{\partial x}\int_0^h dz \int_0^z dz' \int_0^{z'} dz''\, p(x, y, z'', t). \tag{S18}$$

An analogous equation can be derived for the second component of Eq. S5. Upon defining the 2d pressure as:

$$p_{2d}(x, y, t) \equiv \langle p\rangle_z(x, y, t) - \frac{2}{h^3}\int_0^h dz \int_0^z dz' \int_0^{z'} dz''\, p(x, y, z'', t), \tag{S19}$$

we find the following approximation to Eq. S5:

$$-\frac{2\mu}{h^2}\vec{v}_{2d} = \vec{\nabla}_{2d} p_{2d}, \tag{S20}$$

where $\vec{v}_{2d} = (\langle u\rangle_z, \langle v\rangle_z)$ is the 2d velocity given by the 3d velocity components u and v averaged in the z-direction and $\vec{\nabla}_{2d} = (\partial/\partial x, \partial/\partial y)$ is the 2d gradient in the plane (x, y). Eq. S20 is the momentum equation given in the main text (Eq. 4 of the main text), where we dropped the subscript $2d$ for simplicity, given that all functions mentioned in the main text are 2d functions of x and y. This analysis allows us to identify the friction coefficient γ used in the main text with $\gamma = 2\mu/h^2$. The boundary condition for the 2d pressure p_{2d} at the frontier of the colony in the plane (x, y) is $p_{2d} = 2/3\, p_0$, which is a constant, as assumed in the main text.

We can now compute a characteristic length scale above which the approximation holds. Averaging Eq. S5 along the z-direction, we get for the first component of Eq. S5:

$$\mu\left(\frac{\partial^2\langle u\rangle_z}{\partial x^2} + \frac{\partial^2\langle u\rangle_z}{\partial y^2}\right) + \frac{\mu}{h}\int_0^h dz\, \frac{\partial^2 u}{\partial z^2} - \frac{\partial\langle p\rangle_z}{\partial x} = 0. \tag{S21}$$

Averaging Eq. S16 in the z-direction and using Eq. S18, we find:

$$\frac{\mu}{h}\int_0^h dz\, \frac{\partial^2 u}{\partial z^2} = \frac{\partial\langle p\rangle_z}{\partial x} = -\frac{2\mu}{h^2}\langle u\rangle_z + \frac{2}{h^3}\frac{\partial}{\partial x}\int_0^h dz \int_0^z dz' \int_0^{z'} dz''\, p. \tag{S22}$$

Substituting Eq. S22 in Eq. S21 and using the definition of p_{2d} (Eq. S19), and repeating the same calculations for the second component of Eq. S5, we find for the first two components of Eq. S5 averaged along the z-direction in this approximation:

$$\mu\nabla_{2d}^2\vec{v}_{2d} - \frac{2\mu}{h^2}\vec{v}_{2d} = \vec{\nabla}_{2d}p_{2d}, \tag{S23}$$

where ∇_{2d}^2 is the 2d Laplacian. Eq. S23 is Eq. 3 of the main text. The square-root ratio between the coefficients of the friction-like term $-2\mu/h^2\vec{v}_{2d}$ and the viscous-like term $\mu\nabla_{2d}^2\vec{v}_{2d}$ give us a characteristic length-scale l above which the first term can be neglected compared to the second one, as we did in the main text. Our approximation is valid if l is small compared with the other characteristic length-scale in our problem, i.e. the growth layer width δ:

$$l = \sqrt{\mu\frac{h^2}{2\mu}} = \frac{h}{\sqrt{2}} \ll \delta, \tag{S24}$$

which is true for our experiments given that $\sqrt{2}\delta/h \cong 20$.

Generalization to slip boundary condition

The 2d model equations used in the main text hold also if we assume that there is slip between the colony and the agar surface, provided that the characteristic length-scale associated with the slip condition (see below) is small compared with the growth layer width δ. To show this, we replace the no-slip boundary condition (Eq. S6) with Navier-Maxwell slip boundary conditions (5):

$$\begin{aligned} u|_{z=0} &= \zeta\left.\frac{\partial u}{\partial z}\right|_{z=0}, \\ v|_{z=0} &= \zeta\left.\frac{\partial v}{\partial z}\right|_{z=0}, \end{aligned} \tag{S25}$$

where ζ is an extrapolation length at which the no-slip boundary condition would be satisfied below the agar surface (5). Using the boundary conditions in Eq. S25 in place of Eq. S6, one can repeat the calculations made above and find that Eq. S20 is replaced by:

$$-\frac{2\mu}{h(h+2\zeta)}\vec{v}_{2d} = \vec{\nabla}_{2d}p_{2d}, \tag{S26}$$

where p_{2d} is given by:

$$p_{2d}(x,y,t) \equiv \langle p\rangle_z(x,y,t) - \frac{2}{h^2(h+2\zeta)}\int_0^h dz\int_0^z dz'\int_0^{z'} dz''\, p(x,y,z'',t), \tag{S27}$$

which substitutes Eq. S19 (Eqs. S14, S15, S17 and S18 are also modified by the different choice of boundary conditions). Eq. S26 is again of the same form as Eq. 4 of the main text, and the friction coefficient γ with this choice of boundary conditions is equal to $\gamma = 2\mu/[h(h+2\zeta)]$. The criterion for the approximation to be valid now reads:

$$l = \sqrt{\frac{h(h+2\zeta)}{2\mu}} \ll \delta, \tag{S28}$$

which replaces Eq. S24. Thus, assuming slip boundary conditions (Eq. S25), the approximation is valid if both h and ζ are small compared with the growth layer width δ.

9. Boundary condition between the agar and the colony

In the continuum model, we assumed a no-slip boundary condition between the colony and the agar substrate. To show that this boundary condition is reasonable and that friction with the agar substrate dominates over inertial and viscous terms for the bottom-most layer of the colony, we centrifuged two 35 mm Petri dishes filled with 7 mL of 1% agarose YPD medium, on which a yAG2 colony had been grown at 30˚C for 5 days, starting from a 0.6 μL inoculation. Fig. S10 shows that the lowest layer of the colony does not move under the centrifugal force applied, whereas the upper layers of the colony move outwards. The centrifugal acceleration a used (rotor radius 13.5 cm) is shown in Fig. S10C.

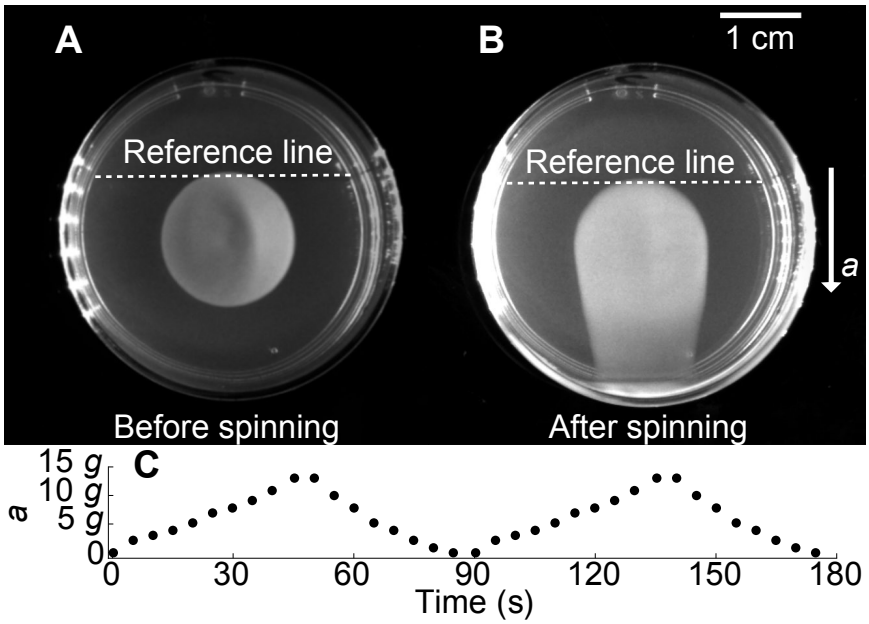

Fig. S10. We grew a colony of yAG2 for 5 days at 30˚C (A) and then spun it (B) with the centrifugal acceleration profile shown in panel C. The symbol g in panel C identifies the acceleration. The arrow in panel B shows the direction of the centrifugal force applied to the colony. Before spinning (A), the colony perimeter was circular and we marked the position of the top edge on the bottom of the Petri dish (white, dashed line). After spinning (B), the lowest layer of the colony in contact with the agar surface shows no movement, whereas the upper layer of cells slide outwards under centrifugal force, in the direction shown by the arrow. The other two replicates were qualitatively similar.

10. Line tension forces

Yeast cells attract each other weakly (25). These attractive forces could, in principle, cause line tension effects at the scale of the colony. We performed the following experiment to show that line tension forces can be neglected in our experimental settings. We inoculated colonies of the heat-sensitive strain yAG20 (*cdc26Δ*) using multiple droplets of an overnight culture, thus initializing colonies with different shapes. We grew these colonies at 28˚C for two days (Fig. S11A and C) and then moved them to 37˚C for a further five days (Fig. S11B and D), to suppress cell division and thus observe possible changes in the colony shapes due to line tension-effects caused by attractive interactions between cells. At the end of the second day of growth at 28˚C, colonies retained their non-circular shapes, including regions of high curvature and these shapes were maintained during the subsequent 5 days at 37˚C. If line tension forces were relevant for our system, high-curvature regions would round out and flatten because of attractive interactions among cells, and the colonies would tend to a circular shape with time. Because such rearrangements were not observed, we conclude that friction with the substrate dominates over line tension terms, which can thus be neglected on the time scales of our experiments. No rearrangements of the upper surface of the colony, including the valleys that formed at the intersection of the circular inoculations (Fig. S11), were observed, suggesting that surface tension forces are negligible in the 3d model as well.

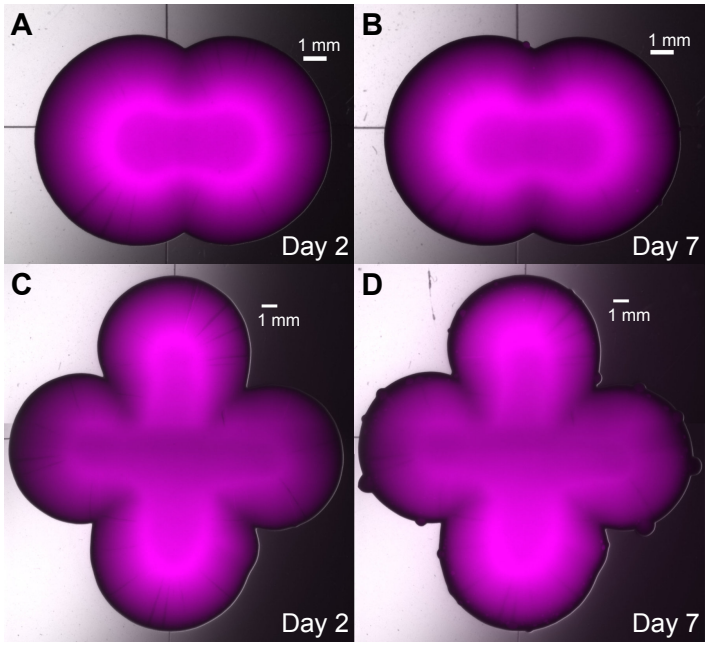

Fig. S11. Colonies of the heat-sensitive strain yAG20 (magenta) were inoculated with various shapes, grown for two days at 28˚C (panel A, two overlapping circular inoculations and panel C, four overlapping circular inoculations) and then moved to 37˚C for a further five days (panels B and D). At 37˚C, the strain yAG20 cannot perform cell-division, which allowed us to test whether changes in the colony shapes due to surface-tension-like forces caused by attractive interactions among cells were relevant in our system. Such changes should be most pronounced in regions of high curvature where the circular boundaries of these colonies intersect. Because no changes in the colonies shapes were observed, we concluded that line tension effects could be neglected in our continuum model on the time scale of our experiments. The small, bulging sectors in panels B and D are spontaneously generated mutants that can grow and divide at 37˚C.

11. Dynamics of sector opening angles in the continuum model

We investigated the dynamics of sector opening angles in the continuum model, by running simulations with different values of the growth layer width, δ, and different values of the initial opening angle, ϕ_0, and the initial radius, r_0. Simulation results show that the dynamics of opening angles do not depend independently of δ, r, and r_0: upon rescaling δ and r by r_0, we found that the dynamics depend only on the ratios δ/r_0 and r/r_0 (Fig. S12), as expected given that this rescaling corresponds to the nondimensionalization of all length scales. Fig. S13 shows that, for fixed r_0 and ϕ_0, the continuum model tends to the constant-speed model for small growth layer widths δ (while keeping the constant asymptotic expansion speeds $\bar{v}_i = \bar{g}_i\delta$ of each strain i constant by varying $\bar{g}_i$), and for large radii (with fixed δ). For fixed values of the growth layer width δ and the initial angle ϕ_0, the rate of increase of the opening angle $d\phi/dr$ tends to the prediction of the constant-speed model when r is large, or equivalently when $\delta/r \ll 1$.

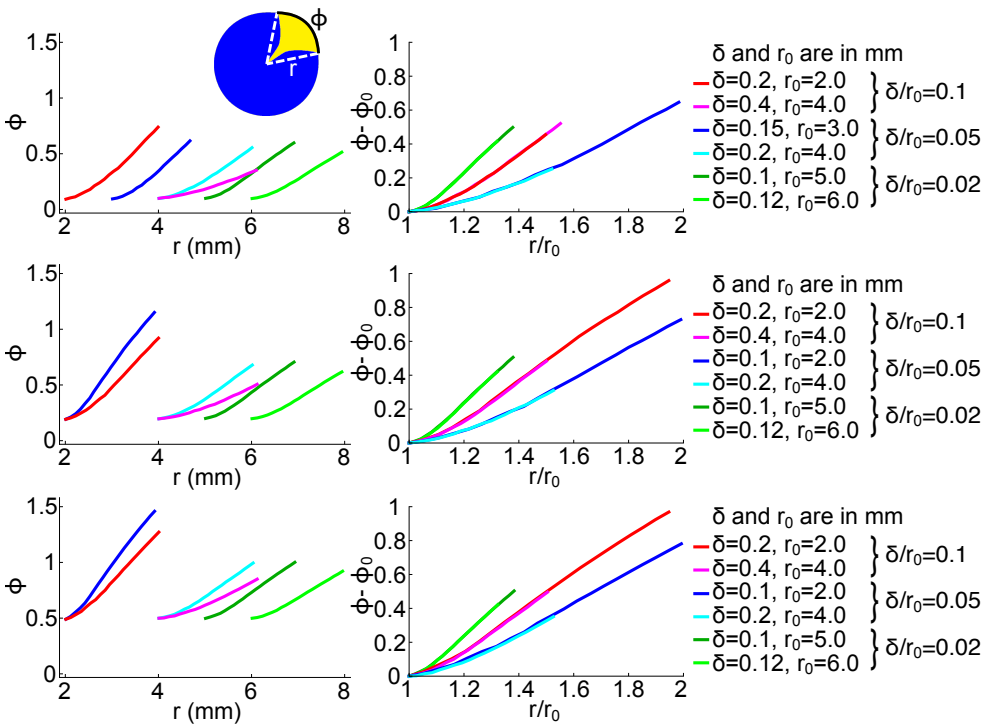

Fig. S12. Opening angles of sweeping sectors in simulations of the continuum model with different values of r_0, ϕ_0 and δ. The inset in the upper left panel is a sketch of a sweeping sector within a colony. The radius r is defined as the radial distance from the center of the colony to the sector boundary (dashed, white lines), i.e. the point at which the two strains meet at the frontier of the colony. The sector opening angle ϕ is the angle formed by the dashed, white lines, subtended by the arc shown in black. The values of the local growth rates $\bar{g}_1$ and $\bar{g}_2$ (with dimensions of 1/time) were set to $\bar{g}_1 = \bar{v}_1/\delta$ and $\bar{g}_2 = \bar{v}_2/\delta$ with fixed $\bar{v}_2 = 1.0$ mm/d and $\bar{v}_2 = 1.5$ mm/d, so that the single-strain asymptotic expansion velocities $\bar{v}_1$ and $\bar{v}_2$ were identical in all simulations. The left column of graphs shows opening angles plotted versus the radial distance r from the center of the colony to the sector boundary, i.e. the point at which the two strains meet at the edge of the colony. The right column of graphs shows the same data with the radii rescaled by the initial radius r_0 and the angles minus the initial angle ϕ_0. Simulations with identical values of δ/r_0 and ϕ_0 collapse. Simulations with different values of ϕ_0 do not collapse (not shown).

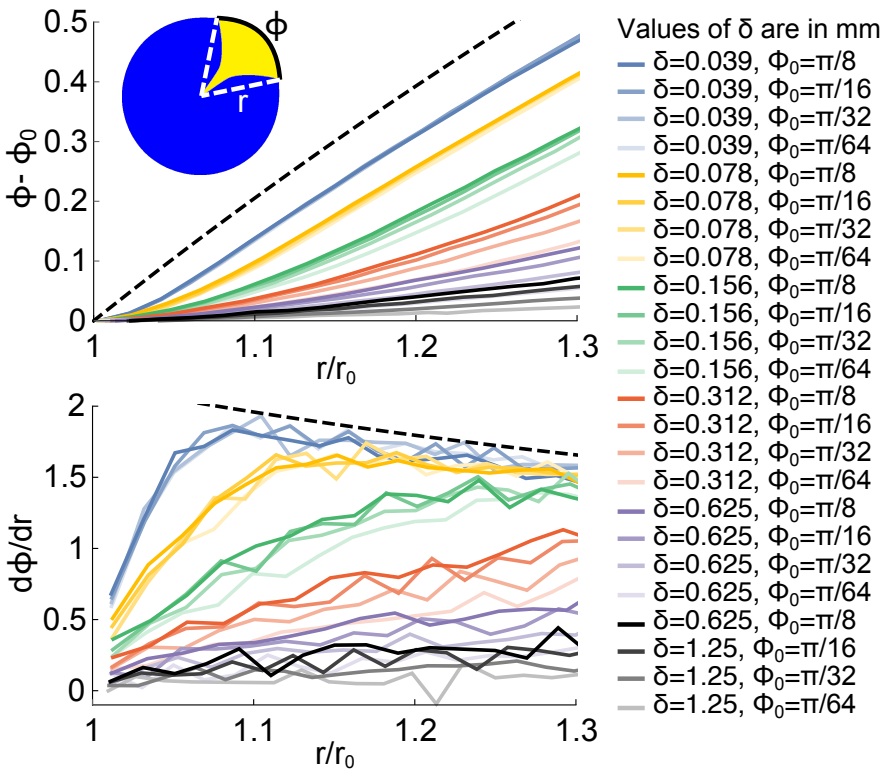

Fig. S13. The continuum model tends to the constant-speed model for small growth layer widths δ, or for large radii (with fixed δ), for constant asymptotic expansion speeds $\bar{v}_1 = \bar{g}_1\delta$ and $\bar{v}_2 = \bar{g}_2\delta$. The inset in the upper panel is a sketch of a sweeping sector within a colony. The radius r is defined as the radial distance from the center of the colony to the sector boundary (dashed, white lines), i.e. the point at which the two strains meet at the frontier of the colony. The sector opening angle ϕ is the angle formed by the dashed, white lines, subtended by the arc shown in black. The upper panel shows the dynamics of opening angles $(\phi - \phi_0)$ in simulations of the continuum model with different values of the growth layer width δ and initial angles ϕ_0 as a function of r/r_0, where r_0 is the radius of the colony in the initial condition. The black dashed line is the prediction of the constant-speed model. As the growth layer width δ decreases, opening angles in the continuum model approach the constant-speed model prediction. For a fixed growth layer width δ (curves with same color of different intensity), the value of $(\phi - \phi_0)$ decreases for smaller values of the initial angle ϕ_0 (curves with colors of smaller intensity have smaller initial angle). The lower panel shows the derivative of the opening angle as a function of r/r_0. The black, dashed line shows the prediction of the constant-speed model for $d\phi/dr$. This plot shows that, for fixed δ and initial angle ϕ_0, the rate of increase of the opening angle $d\phi/dr$ tends to the constant-speed model prediction when r is large, consistent with the condition $\delta/r \ll 1$. Parameters were set to $\bar{v}_1 = \bar{g}_1\delta = 1.0$ mm/d (by varying $\bar{g}_1$ for different values of δ), $\bar{v}_2 = \bar{g}_2\delta = 1.5$ mm/d (by varying $\bar{g}_2$ for different values of δ) and $r_0 = 5$ mm.

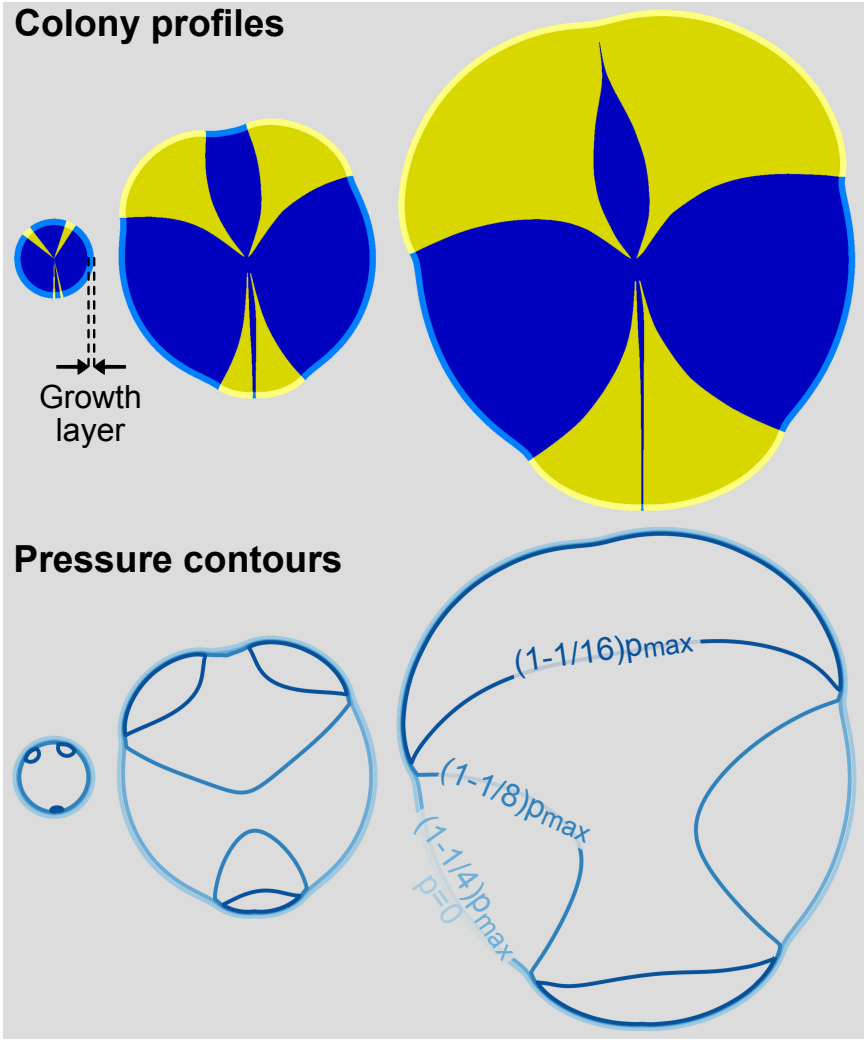

Fig. S14. Numerical integration of the continuum model, starting from the initial condition shown as the small upper-left image. This is the same colony as the one shown in Fig. 4B. The spatial distribution of the slower-growing (blue) and the faster-growing (yellow) strains are shown in the first row, at different times. The actively-growing layers are shown in light yellow or light blue. The second row shows pressure contours at different times. Shown are the contours $p = 0$ (lightest blue), $p = (1 - 1/4)p_{max}$, $p = (1 - 1/8)p_{max}$ and $p = (1 - 1/16)p_{max}$, where p_{max} was evaluated at each time step.

Caption for Movie S1

Non-proliferating, heat-sensitive cells (magenta) can be pulled outwards by a proliferating (cyan) strain and form thin filaments similar to those shown in Fig. 1A. Each frame is a combined fluorescent and bright-field image of the same colony shown in Fig. 1B-C-C1 and Fig. S2C during growth at 37˚C. The non-heat-sensitive strain yAG19 (cyan, initial frequency 10%) and the heat-sensitive strain yAG20 (magenta, initial frequency 90%) were grown at 28˚C for two days and subsequently imaged every 10 min with a stereoscope incubated at 37˚C, a temperature at which yAG20 cells cannot divide. The video starts 3 h after the move to 37˚C and lasts for 20 h (time is displayed as hh:mm). The strain yAG20 (magenta) stops expanding after 9 h at 37˚C (Fig. S2D). The right panel shows the right edge of the colony in the fluorescent channel corresponding to the strain yAG20 (magenta on the left, white on the right), overexposed to highlight the displacement of the non-proliferating strain yAG20 (white) by the proliferating strain yAG19 (dark).

References

1. Stearns T, Hoyt MA, Botstein D (1990) Yeast mutants sensitive to antimicrotubule drugs define three genes that affect microtubule function. *Genetics* 124(2):251-262.
2. Osher S, Fedkiw RP (2003) *Level set methods and dynamic implicit surfaces* (Springer, New York).
3. Thampi SP, Ansumali S, Adhikari R, Succi S (2013) Isotropic discrete laplacian operators from lattice hydrodynamics. *J Comput Phys* 234:1-7.
4. Korolev KS, *et al*. (2012) Selective sweeps in growing microbial colonies. *Phys Biol* 9:026008.
5. Lauga E, Brenner MP, Stone HA (2007) Microfluidics: The No-Slip Boundary Condition. *Springer Handbook of Experimental Fluid Mechanics*, eds Tropea C, Yarin AL, Foss JF (Springer, Berlin).